Analysis and application of an overlapped FEM-BEM for wave propagation in unbounded and heterogeneous media

V. Domínguez * M. Ganesh †

June 30, 2021

Dedicated to the memory of Francisco-Javier "Pancho" Sayas (1968-2019).

Abstract

An overlapped continuous model framework, for the Helmholtz wave propagation problem in unbounded regions comprising bounded heterogeneous media, was recently introduced and analyzed by the authors (J. Comput. Phys., **403**, 109052, 2020). The continuous Helmholtz system incorporates a radiation condition (RC) and our equivalent hybrid framework facilitates application of widely used finite element methods (FEM) and boundary element methods (BEM), and the resulting discrete systems retain the RC exactly. The FEM and BEM discretizations, respectively, applied to the designed interior heterogeneous and exterior homogeneous media Helmholtz systems include the FEM and BEM solutions matching in artificial interface domains, and allow for computations of the exact ansatz based far-fields. In this article we present rigorous numerical analysis of a discrete two-dimensional FEM-BEM overlapped coupling implementation of the algorithm. We also demonstrate the efficiency of our discrete FEM-BEM framework and analysis using numerical experiments, including applications to non-convex heterogeneous multiple particle Janus configurations. Simulations of the far-field induced differential scattering cross sections (DSCS) of heterogeneous configurations and orientation-averaged (OA) counterparts are important for several applications, including inverse wave problems. Our robust FEM-BEM framework facilitates computations of such quantities of interest, without boundedness or homogeneity or shape restrictions on the wave propagation model.

AMS subject classifications: 65N30, 65N38, 65F10, 35J05

Keywords: Helmholtz, Heterogeneous, Unbounded, Wave Propagation, Finite Element Methods, Integral Equations, Nyström Boundary Element Methods, Janus Configurations

*Department of Estadística, Informática y Matemáticas, Universidad Pública de Navarra, Tudela, Spain/ Institute for Advanced Materials (INAMAT), Pamplona, Spain. Email: victor.dominguez@unavarra.es

†Department Applied Mathematics and Statistics Department, Colorado School of Mines, Golden, CO, USA. Email: mganesh@mines.edu

1 Introduction

Simulation of scattered acoustic and electromagnetic fields, and hence understanding the impact of refractive indices of wave propagation media, are crucial for a large class of applications [6, 24, 31, 33]. The term *Janus particles* was mentioned in a Nobel Prize lecture [9] about three decades ago, and since then additional interests include understanding the effect of a class of piecewise-continuous heterogeneous refractive indices induced Janus configurations. A simple Janus particle is designed by combining two distinct homogeneous refractive indices, and Janus configurations in general may comprise multiple particles or complex structures with heterogeneous material properties. The example configuration Ω_0, of the type illustrated in Figure 1, has been investigated for synthesis and applications, see for example [29, 34, 38, 39].

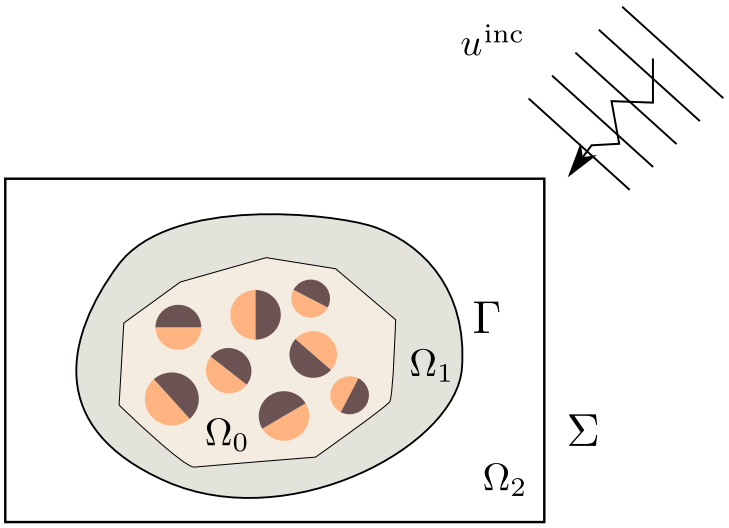

Figure 1: *An incident wave u^{inc} impinging on a given Janus-type heterogeneous multiple-particle configuration (Ω_0) in $\mathbb{R}^2$. Our framework introduces two artificial boundaries Σ and Γ, and hence two overlapped computational regions: (i) a bounded FEM-domain Ω_2 (with boundary Σ) and (ii) an unbounded BEM-region $\mathbb{R}^2 \setminus \overline{\Omega}_1$ (exterior to the smooth interface Γ). The FEM and BEM solutions are constrained to match in the overlapped region $\Omega_{12} := (\mathbb{R}^2 \setminus \overline{\Omega}_1) \cap \Omega_2$.*

Developing numerical methods to understand scattering effects by Janus configurations (even with simple structures) has been an active area of research, see for example the Janus spherical acoustic configuration effect research [21, 33] published in 2020 and references therein. Motivated by details in the book [33], authors of [21] numerically investigated scattering effects of homogeneous spheres with two standard (sound-soft and transmission) boundary properties, leading to solving the Helmholtz equation with two distinct boundary conditions and the Sommerfeld radiation condition (SRC), for the unknown scattered- and far-fields.

As described in [21, 33], to understand the impact of Janus-type wave configurations, accurate simulations of certain quantities of interests (QoI) are important. The two key QoI are the far-field intensity based differential scattering cross sections (DSCS) and also the configuration orientation effect QoI, the orientation-averaged (OA) DSCS. Simulation of the OA-DSCS is equivalent to simulating far-fields generated by the configuration, such as Ω_0 in Figure 1, with the incident wave u^{inc} impinging Ω_0 from hundreds of directions surrounding the configuration. The key numerical tool in [21] is the stable far-fields based T-matrix framework that was analyzed (with *a priori bounds*) and implemented in [13, 14]. For nonlinear inverse problems based

applications that use the far-field (with phase or phase-less DSCS) data, efficient simulation of far-fields (such as at each Newton-type iterations) are important, see for example the 2019 book [6] and extensive references therein.

Far-field computations based numerical schemes for such QoI and tools, in general, do not allow for configurations with heterogeneous structures and unbounded regions. This is mainly because numerical partial differential equation (PDE) algorithms mainly apply either the ubiquitous finite element method (FEM) or the boundary element method (BEM). The FEM requires a bounded domain for finite number of tessellations, and the BEM requirement of the fundamental solution is practical mainly for a homogeneous medium PDE. The FEM is applied to a variational formulation equation of the PDE that involves domain integrals, and the BEM discretizes an equivalent boundary integral equation (BIE) for the boundary unknown in a chosen ansatz for the scattered field, in conjunction with the fundamental solution [6, 31].

Accordingly for wave propagation models with a bounded heterogeneous medium (Ω_0), to apply the FEM, an artificial truncation of the unbounded region using, typically, a polygonal boundary Σ (as in Figure 1) is introduced and a wave absorbing boundary condition (ABC) on Σ is imposed, ignoring the SRC. The standard variational formulation on the boundary polygonal domain (such as Ω_2 in Figure 1) for the heterogeneous Helmholtz PDE with ABC on Σ is sign-indefinite [16,24] and this non-coercive restriction was removed recently by developing, analyzing, and implementing a new sign-definite variational formulation [17]. Another option to exactly incorporate the SRC is, for example, by ignoring the heterogeneity and consider instead the homogeneous model exterior to the polygonal boundary Σ or exterior to a smooth boundary Γ (as in Figure 1). The artificial smooth boundary choice is especially suitable for developing high-order spectrally accurate approximation of the scattered field in the homogeneous medium using high-order BEMs.

For Janus-type configurations, it is important to avoid restrictions in either of the above two options by using both the FEM and BEM. This can be achieved by appropriately coupling the FEM and BEM solutions, depending on the choices of the artificial boundaries to compute the interior (heterogeneous) and exterior (homogeneous) media solutions. Such FEM-BEM coupling mathematical frameworks have been developed and analyzed only by a few authors, but several researchers implemented the associated FEM-BEM computational frameworks.

The widely used FEM-BEM coupling is obtained by choosing one artificial (FEM appropriate) polygonal boundary Σ, see for example the review article [36] and references therein. In addition to analysis difficulties [36], this approach introduces restricted regularity for the solution exterior to Σ. The high-order regularity based (BEM appropriate) single smooth boundary choice Γ was subsequently developed in [26, 27]. For recent implementations of the single artificial boundary based FEM-BEM framework with high-order accuracy we refer to [15, 16, 19], and associated analysis issues are highlighted in [15, Section 6]. Using two artificial interfaces a mathematical framework was developed over four decades ago in [25] and was subsequently used in [8, 22]. A domain-overlapped framework [illustrated in Figure 1 with overlapped region $(\mathbb{R}^2 \setminus \overline{\Omega}_1) \cap \Omega_2$] was developed recently by the authors in [10] that takes advantage of a polygonal boundary (Σ) required for a wide-class FEM, and a smooth boundary (Γ) for high-order spectral BEM. Mathematical analysis of the continuous framework in [10] establishes the equivalence and regularity of the decomposed model.

In this work we present rigorous numerical analysis of the FEM-BEM adaptive coupling framework introduced in [10] for solving the Helmholtz acoustic/electromagnetic wave propagation problem on the plane with a bounded heterogeneous region, and demonstrate efficiency

of the numerical algorithm for complex Janus-type heterogeneous configurations with computational experiments. The algorithm works on a suitable partition of the plane defined from a polygonal domain containing a smooth curve that surround all heterogeneity. The overlapped partition is made up of the bounded polygonal domain containing the heterogeneity, and the unbounded homogeneous region exterior to the smooth curve.

On the bounded domain of the partition we approximate the solution by a FEM with classical continuous piecewise polynomials on triangular grids, whereas a high-order Nyström BEM is used to compute the scattered wave in the unbounded region. Both solutions are coupled by demanding to coincide in the two artificial boundaries that ensures the FEM and BEM solutions matching in the intersecting common domain of the partition. We prove that the convergence of the scheme in natural norms is of the same order as the best approximations of the projection in the FEM and BEM finite dimensional spaces. In addition, since the Nyström method is super-algebraically convergent, only a relatively few degrees of freedom are required in the BEM solver to keep the error of the same order as the FEM solution, and hence the algorithm facilitates accurate far field, DSCS, and OA-DSCS computations.

The rest of this article is organized as follows: In Section 2, we recall the Helmholtz model and an equivalent decomposition decomposition framework, both at continuous level. In Section 3 we setup a discrete counterpart of the decomposition framework and the overlapped FEM-BEM algorithm. Rigorous numerical analysis of the FEM-BEM algorithm establishing optimal order convergence, of the hybridized numerical solutions, in Section 4 forms the main theoretical contribution of the article that include references to several results proven in the two Appendix sections of this article. In Section 5, we computationally demonstrate the described algorithm and theoretically analysis using three distinct sets of experiments, in conjunction with the theory and practical applicability, including implementation of the algorithm for multiple-particle Janus-type configurations with non-smooth solutions, and also for complex structured heterogeneous regions.

2 Helmholtz model and decomposition framework

Throughout the article, let n be a piecewise-continuous refractive index with heterogeneity restricted to a bounded domain $\Omega_0 \subset \mathbb{R}^2$, and in the exterior we take $n|_{\Omega_0^c} \equiv 1$ so that the exterior Ω_0^c ($:= \mathbb{R}^2 \setminus \overline{\Omega_0}$) is a free-space unbounded medium.

The scattered field u^s is induced by an incident wave $u^{\rm inc}$ (with wavenumber $k > 0$) from the exterior region impinging on the heterogeneous medium Ω_0. It is convenient to assume that that incident field satisfies the homogeneous Helmholtz equation $\Delta v + k^2 v = 0$ in all of the plane $\mathbb{R}^2$, although it is sufficient to take it to satisfy outside of a compact set in $\mathbb{R}^2$ containing, say, a point-source. Physically appropriate incident waves such as the plane-wave and point-source have these properties.

We seek the total wave field u ($:= u^s + u^{\rm inc}$) $\in H^1_{\rm loc}(\mathbb{R}^2)$, representing acoustic or electromagnetic fields, satisfying the uniquely solvable problem governed by the variable coefficient Helmholtz equation and the SRC (with $\widehat{\boldsymbol{x}} := \boldsymbol{x}/|\boldsymbol{x}| \in \mathbb{S}^1$):

$$\left|\begin{array}{rcl} \Delta u + k^2 n^2\, u &=& 0, \quad \text{in } \mathbb{R}^2, \\ \partial_{\widehat{\boldsymbol{x}}} u^s - \mathrm{i}k u^s &=& o(|\boldsymbol{x}|^{-1/2}), \quad \text{as } |\boldsymbol{x}| \to \infty. \end{array}\right. \tag{2.1}$$

We note that in the heterogeneous medium Ω_0, u^s is the interior unknown field and is the solution of inhomogeneous Helmholtz equation with inhomogeneous term $f = -(\Delta u^{\rm inc} + k^2 n^2\, u^{\rm inc})$.

For the unknown scattered field u^s exterior to Ω_0, in (2.1), the SRC

$$\lim_{|\boldsymbol{x}|\to\infty} |\boldsymbol{x}|^{1/2} \left(\frac{\partial u^s(\boldsymbol{x})}{\partial \widehat{\boldsymbol{x}}} - \mathrm{i}k u^s(\boldsymbol{x}) \right) = 0. \tag{2.2}$$

holds uniformly in all directions $\widehat{\boldsymbol{x}} = \boldsymbol{x}/|\boldsymbol{x}| \in \mathbb{S}^1$. The scattered field u^s is a radiating field and, as a consequence of the SRC, its behavior at infinity is captured by the far-field $u^\infty \in L^2(\mathbb{S}^1)$, where

$$u^\infty(\widehat{\boldsymbol{x}}) = \lim_{|\boldsymbol{x}|\to\infty} |\boldsymbol{x}|^{1/2} e^{-\mathrm{i}k|\boldsymbol{x}|} u^s(\boldsymbol{x}). \tag{2.3}$$

For the total field u induced by a plane wave with incident direction $\widehat{\boldsymbol{d}} \in \mathbb{S}^1$, it is appropriate to denote the associated far-field as $u^\infty(\widehat{\boldsymbol{x}}; \widehat{\boldsymbol{d}}) = u^\infty(\theta; \phi)$, with $\widehat{\boldsymbol{x}} = p(\theta) = (\cos\theta, \sin\theta)$ and $\widehat{\boldsymbol{d}} = p(\phi) = (\cos\phi, \sin\phi)$, for some $\theta, \phi \in [0, 2\pi)$. The single-incident plane wave QoI DSCS and multiple-incident plane waves QoI OA-DSCS are then given by [21, 33]

$$u_{\mathrm{DSCS}}(\theta;\phi) = |u^\infty(\theta;\phi)|^2; \qquad u^{\mathrm{OA}}_{\mathrm{DSCS}}(\theta) = \frac{1}{2\pi}\int_0^{2\pi} |u^\infty(\theta;\phi)|^2 \,\mathrm{d}\phi. \tag{2.4}$$

Clearly, computation of the $u^{\mathrm{OA}}_{\mathrm{DSCS}}$ with high-accuracy requires discretization of the above integral with over thousand discrete incident direction angles ϕ, leading to solving the same number of Helmholtz model (2.1)-(2.2) for many distinct inputs. This motivates the difficulty of evaluating $u^{\mathrm{OA}}_{\mathrm{DSCS}}$ Janus-type configurations with piecewise-continuous refractive indices defined on non-trivial geometries.

For the given wave propagation problem (2.1), next we recall an equivalent decomposition framework introduced and analyzed in [10]. The framework introduce two artificial curves Γ and Σ with interior Ω_1 and Ω_2, respectively, satisfying $\overline{\Omega}_0 \subset \Omega_1 \subset \overline{\Omega}_1 \subset \Omega_2$, with the assumption that Γ is smooth and Σ is a polygonal boundary. A sketch of the different domains is displayed in Figure 1. We denote henceforth $\Omega_1^{\mathrm{c}} := \mathbb{R}^2 \setminus \overline{\Omega}_1$. At continuous level, it is convenient to consider the decomposition framework using operators defined on classical Sobolev spaces. To this end, for a general domain $D \in \mathbb{R}^2$ with boundary ∂D and for real m, let $H^m(D)$ denote the classical Sobolev space.

We also consider $H^s(\partial D)$ which is well defined for any s if D is smooth. Recall that in this case the trace operator $\gamma_{\partial D} : H^{s+1/2}(D) \to H^s(\partial D)$ is continuous for any $s > 0$ as consequence of the Sobolev Trace Theorems, see for example [7] or [30, Ch 4].

For Lipschitz domains Ω with boundary $\Sigma = \partial\Omega$, such as the chosen polygonal domain Ω_2, $H^s(\Sigma)$ is defined only for $s \in [-1, 1]$ [1, 20, 30]. We then commit a (slight) abuse of notation and set for $s > 1$

$$H^s(\Sigma) = \left\{ \gamma_\Sigma u \ : \ u \in H^{s+1/2}(D) \right\}. \tag{2.5}$$

In (2.5) the open domain D is chosen such that $\Sigma \subset \overline{D}$, and the space is endowed with the image norm. It is known that the space is independent of D and, for $s \in (0, 1)$, it is a classical Sobolev space. Thus, using the definitions, the trace operator $\gamma_\Sigma : H^{s+1/2}(D) \to H^s(\Sigma)$ is continuous for $s \in (0, 1) \cup (1, \infty)$.

The decomposition framework starts with an interior and an exterior Helmholtz problem:

- (**Interior Dirichlet Helmholtz problem in Ω_2 with polygonal boundary Σ**): Given $f_\Sigma \in H^{1/2}(\Sigma)$, find $\omega_{\mathrm{int}} \in H^1(\Omega_2)$ so that

$$\left| \begin{array}{rcll} \Delta\omega_{\mathrm{int}} + k^2 n^2 \, \omega_{\mathrm{int}} & = & 0, & \text{in } \Omega_2, \\ \gamma_\Sigma \omega_{\mathrm{int}} & = & f_\Sigma. & \end{array} \right. \tag{2.6}$$

- (**Exterior Dirichlet Helmholtz problem in Ω_1^c with smooth boundary Γ**): Given $f_\Gamma \in H^{1/2}(\Gamma)$, find $\omega_{\text{ext}} \in H^1_{\text{loc}}(\Omega_1^c)$ so that

$$\left|\begin{array}{rcll} \Delta\omega_{\text{ext}} + k^2\omega_{\text{ext}} &=& 0, & \text{in } \Omega_1^c, \\ \gamma_\Gamma\omega_{\text{ext}} &=& f_\Gamma, & \\ \partial_{\widehat{\boldsymbol{x}}}\omega_{\text{ext}} - \mathrm{i}k\omega_{\text{ext}} &=& o(|\boldsymbol{x}|^{-1/2}). & \end{array}\right. \tag{2.7}$$

The SRC in (2.7) ensures that the exterior Dirichlet problem is uniquely solvable [6, 31] for all wavenumbers k. For the interior Dirichlet Helmholtz problem (2.6) the well-posedness does not hold for all wavenumbers k [24], and throughout this article we assume that the wavenumber k is such that ω_{int} is the unique solution of (2.6). The well-posedness assumption for the interior Dirichlet Helmholtz problems in Ω_2 (and in the overlapped region $\Omega_{12} := \Omega_1^c \cap \Omega_2$) can be easily avoided, for example, by modifying the artificial boundaries Σ and Γ [10, Section 2.1].

It is convenient to use operators to describe the continuous decomposition framework. To this end, corresponding to the interior Dirichlet problem (2.6) we consider two operators $\mathrm{K}_{\Omega_2\Sigma}, \mathrm{K}_{\Gamma\Sigma}$; and associated with the exterior problem (2.7) we consider two operators $\mathrm{K}_{\Omega_1^c\Gamma}, \mathrm{K}_{\Sigma\Gamma}$. These pairs of operators are defined, using the unique solution ω_{int} of (2.6) and ω_{ext} of (2.7) and their traces respectively on Γ and Σ, as follows:

$$\mathrm{K}_{\Omega_2\Sigma} f_\Sigma = \omega_{\text{int}}, \qquad \mathrm{K}_{\Gamma\Sigma} f_\Sigma = \gamma_\Gamma\omega_{\text{int}}; \qquad\qquad \mathrm{K}_{\Omega_1^c\Gamma} f_\Gamma = \omega_{\text{ext}}, \quad \mathrm{K}_{\Sigma\Gamma} f_\Gamma = \gamma_\Sigma\omega_{\text{ext}}. \tag{2.8}$$

In [10], the authors proved that the unique solution u of (2.1) can be constructed in two steps as follows:

1. Find $f_\Sigma : \Sigma \to \mathbb{C}$ and $f_\Gamma : \Gamma \to \mathbb{C}$ so that

$$\left|\begin{array}{rcrcl} f_\Sigma & - & \mathrm{K}_{\Sigma\Gamma} f_\Gamma & = & \gamma_\Sigma u^{\text{inc}}, \\ -\mathrm{K}_{\Gamma\Sigma} f_\Sigma & + & f_\Gamma & = & -\gamma_\Gamma u^{\text{inc}}. \end{array}\right. \tag{2.9a}$$

2. Construct

$$u = \begin{cases} \mathrm{K}_{\Omega_2\Sigma} f_\Sigma, & \text{in } \Omega_2, \\ \mathrm{K}_{\Omega_1^c\Gamma} f_\Gamma + u^{\text{inc}}, & \text{in } \Omega_1^c. \end{cases} \tag{2.9b}$$

The boundary unknowns system (2.9a) can be written in matrix-valued operator form as

$$(\mathcal{I} - \mathcal{K}) \begin{bmatrix} f_\Sigma \\ f_\Gamma \end{bmatrix} = \begin{bmatrix} \gamma_\Sigma u^{\text{inc}} \\ -\gamma_\Gamma u^{\text{inc}} \end{bmatrix}, \qquad \mathcal{K} := \begin{bmatrix} & \mathrm{K}_{\Sigma\Gamma} \\ \mathrm{K}_{\Gamma\Sigma} & \end{bmatrix}. \tag{2.10}$$

($\mathcal{I}$ is obviously the identity matrix operator.) It is not difficult to see that the off-diagonal block $\mathcal{K} : H^0(\Sigma) \times H^0(\Gamma) \to H^s(\Sigma) \times H^s(\Gamma)$ is continuous for any $s \geq 0$ [10].

The following result summarizes the equivalence of the decomposition framework to the original problem (2.1) at the continuous level.

Theorem 2.1. *Assume that the only solution to problem*

$$\left|\begin{array}{rcll} \Delta v + k^2 v &=& 0, & \text{in } \Omega_{12} = \Omega_1 \cap \Omega_2^c, \\ \gamma_\Gamma v &=& 0, & \gamma_\Sigma v = 0 \end{array}\right. \tag{2.11}$$

is the trivial one. Then $\mathcal{I} - \mathcal{K} : H^s(\Sigma) \times H^s(\Gamma) \to H^s(\Sigma) \times H^s(\Gamma)$ is invertible for any $s \geq 0$. Therefore (2.9a) is uniquely solvable. Furthermore, u defined by (2.9b) is the unique solution of the full Helmholtz problem (2.1).

Proof. This result is proven in [10]. We will give here a sketch of the proof for the sake of completeness. By Fredholm alternative it suffices to show that $\mathcal{I}-\mathcal{K}$ is one-to-one. We note that any if $(f_\Sigma^*, f_\Gamma^*) \in N(\mathcal{I}-\mathcal{K})$ then $\omega_{12} := (\mathrm{K}_{\Omega_2\Sigma} f_\Sigma^* - \mathrm{K}_{\Omega_1^c\Gamma} f_\Gamma^*)|_{\Omega_{12}}$ is a solution for (2.11). By hypothesis, $\omega_{12}=0$. Hence, u in (2.9b) is well defined for $u^{\mathrm{inc}}=0$. The well-posedness of the scattering problem (2.1), implies that $u=0$. In particular, $\mathrm{K}_{\Omega_1^c\Gamma} f_\Gamma^*|_{\Omega_2^c}=0$, and from the analytic continuation principle $\mathrm{K}_{\Omega_1^c\Gamma} f_\Gamma^\star = 0$. Therefore, also $\mathrm{K}_{\Omega_2\Sigma} f_\Sigma^*|_{\Omega_{12}}=0$ and hence $(f_\Sigma^*, f_\Gamma^*)=\mathbf{0}$. □

Remark 2.2. For the OA-DSCS calculations with a large number of incident plane waves u^{inc}, a marked advantage of our equivalent formulation (2.9a)-(2.9b) compared to the original model problem (2.1) [with a large number of inhomogeneous terms $f=-(\Delta u^{\mathrm{inc}}+k^2n^2\,u^{\mathrm{inc}})$ in Ω_0] is that the interior and exterior homogeneous problems $\mathrm{K}_{\Omega_2\Sigma} f_\Sigma, \mathrm{K}_{\Omega_1^c\Gamma} f_\Gamma$ (and hence their traces $\mathrm{K}_{\Gamma\Sigma} f_\Sigma, \mathrm{K}_{\Sigma\Gamma} f_\Gamma$) can be setup *independently* of the incident waves. Since the unknowns f_Σ and f_Γ are defined, respectively, only on boundary curves Σ and Γ, these unknowns can represented by a few boundary unknowns (or boundary basis functions) and hence the associated Helmholtz problems setup $\mathrm{K}_{\Omega_2\Sigma} f_\Sigma, \mathrm{K}_{\Omega_1^c\Gamma} f_\Gamma$ is a *naturally parallel* process for computational purposes.

3 Discrete decomposition FEM-BEM framework

The numerical discretization of the continuous decomposition framework (2.9) is essentially obtained by replacing the four continuous operators in (2.8) using appropriate FEM and BEM based discrete counterparts. For $\mathrm{K}_{\Omega_2\Sigma}$ we will use the standard FEM with continuous piecewise polynomial elements on a triangular conformal mesh of Ω_2 [24].

For the BEM certainly an extensive range of methods is at our disposal in the literature [6, 31]. We will restrict ourselves to the spectrally accurate Nyström method [6, 28] .This scheme provides a discretization of the key boundary integral operators of the associated Calderon calculus; in this article we will use only make use of the discrete Single- and Double-Layer operators that converge super-algebraically, and it is not difficult to implement. A disadvantage of the Nyström method is that it requires an accurate differentiable parameterization of the boundary. This is because the method is based on splitting the integral operators into regular and singular parts for which appropriate decompositions and factorizations of the kernels of the operators are needed. This is not a severe restriction in our case since Γ is an auxiliary user-chosen artificial curve and therefore can be taken to be simple and smooth.

In the next two subsections we recall the standard FEM and Nyström procedure and conclude this section with the discrete FEM-BEM decomposition framework required for the main focus of this work on the numerical analysis of the FEM-BEM algorithm [10] .

The FEM procedure

Let $\{\mathcal{T}_h\}_h$ be a sequence of regular triangular meshes with h denoting the discrete parameter, the diameter of the largest element of the grid. We then write $h\to 0$ to mean that the maximum of the diameters of the elements tends to 0. A technical mesh assumption, not restrictive in practice, described in detail in Assumption 1 below, will be used in our proofs to ensure (i) a faster convergence of the FEM in stronger norms around Γ (see Theorem B.1 in Appendix); and (ii) the stability of the full method.

On $\mathcal{T}_h$, we construct the finite dimensional FEM space

$$\mathbb{P}_{h,d} := \{v_h \in \mathcal{C}^0(\Omega_2) : \ u_h|_{T_h} \in \mathbb{P}_d, \ \forall T_h \in \mathcal{T}_h\},$$

where $\mathbb{P}_d$ is the space of bivariate polynomial of degree d. Then given $f_\Sigma^h \in \gamma_\Sigma \mathbb{P}_{h,d}$, we define

$$\mathrm{K}^h_{\Omega_2\Sigma} : \gamma_\Sigma \mathbb{P}_{h,d} \to \mathbb{P}_{h,d}$$

as $\mathrm{K}^h_{\Omega_2\Sigma} f_\Sigma^h := u_h$ that is the unique of the standard FEM discrete system:

$$\left|\begin{array}{l} u_h \in \mathbb{P}_{h,d} \\ b_{k,n}(u_h, v_h) = 0, \quad \forall v_h \in \mathbb{P}_{h,d} \cap H^1_0(\Omega_2) \\ \gamma_\Sigma u_h = f_\Sigma^h, \end{array}\right. \qquad b_{k,n}(u,v) := \int_{\Omega_2} \nabla u \cdot \nabla v - k^2 \int_{\Omega_2} n^2\, uv. \quad (3.1)$$

It is well known that $\mathrm{K}^h_{\Omega_2\Sigma}$ [24] is well defined for any sufficiently fine mesh. Notice also that $\mathrm{K}^h_{\Omega_2\Sigma}$ is defined on the discrete space $\gamma_\Sigma \mathbb{P}_{h,d}$, the trace finite element space on the boundary Σ. Hence, with the help of

$$\mathrm{Q}^h_\Sigma : \mathcal{C}^0(\Sigma) \to \gamma_\Sigma \mathbb{P}_{h,d}, \quad (3.2)$$

the nodal interpolation operator on $\gamma_\Sigma \mathbb{P}_{h,d}$ defined by the finite element space, we have

$$\mathrm{K}^h_{\Omega_2\Sigma} \mathrm{Q}^h_\Sigma \approx \mathrm{K}_{\Omega_2\Sigma},$$

providing an optimal approximation in $\mathbb{P}_{h,d}$ for sufficiently smooth Dirichlet data f_Σ^h (see Theorem 4.1 in the next section).

The BEM procedure

Let

$$\mathbf{x} = (x_1(t), x_2(t)) : \mathbb{R} \to \Gamma \quad (3.3)$$

be a smooth $2\pi-$periodic parameterization of Γ. We denote by SL_k, DL_k, the (parameterized) layer potentials, defined for $\boldsymbol{z} \in \mathbb{R}^2 \setminus \Gamma$ as,

$$\begin{aligned} (\mathrm{SL}_k \varphi_{\mathrm{per}})(\boldsymbol{z}) &:= \int_0^{2\pi} \Phi_k(\boldsymbol{z} - \mathbf{x}(t)) \varphi_{\mathrm{per}}(t)\, \mathrm{d}t, \\ (\mathrm{DL}_k g_{\mathrm{per}})(\boldsymbol{z}) &:= \int_0^{2\pi} \big(\nabla_{\boldsymbol{y}} \Phi_k(\boldsymbol{z} - \boldsymbol{y})\big)\Big|_{\boldsymbol{y}=\mathbf{x}(t)} \cdot \boldsymbol{\nu}(t)\, g_{\mathrm{per}}(t)\, \mathrm{d}t, \end{aligned}$$

where $\Phi_k = \frac{\mathrm{i}}{4} H_0^{(1)}(k|\cdot|)$ is the fundamental solution for the constant coefficient Helmholtz operator in $\mathbb{R}^2$ with wavenumber k; $\boldsymbol{\nu}(t) := (x_2'(t), -x_1'(t))$ is a non-normalized normal vector. Observe that $|\mathbf{x}'(t)| > 0$ is then incorporated to the density in SL_k and to the kernel in DL_k. We follow the same convention for the single and double boundary operator defined for 2π-periodic densities φ_{per} and g_{per} as

$$(\mathrm{V}_k \varphi_{\mathrm{per}})(s) := \ (\gamma_\Gamma \mathrm{SL}_k \varphi_{\mathrm{per}})(\mathbf{x}(s)) = \int_0^{2\pi} \Phi_k(\mathbf{x}(s) - \mathbf{x}(t)) \varphi_{\mathrm{per}}(t)\, \mathrm{d}t \quad (3.4)$$

$$(\mathrm{K}_k g_{\mathrm{per}})(s) := \ \pm\tfrac{1}{2} g_{\mathrm{per}}(s) + (\gamma_\Gamma^{\mp} \mathrm{DL}_k g_{\mathrm{per}})(s) = \int_0^{2\pi} \big(\nabla_{\boldsymbol{y}} \Phi_k(\mathbf{x}(s) - \boldsymbol{y})\big)\Big|_{\boldsymbol{y}=\mathbf{x}(t)} \cdot \boldsymbol{\nu}(t)\, g_{\mathrm{per}}(t)\, \mathrm{d}t. \quad (3.5)$$

The Brakhage-Werner formulation, first introduced in [3] (see also [6, 31]) provides a robust representation for the solution of the exterior Dirichlet solution for the Helmholtz problem (2.7):

$$\mathrm{K}_{\Omega_1^c\Gamma} f_\Gamma = (\mathrm{DL}_k - \mathrm{i}k\mathrm{SL}_k)(\tfrac{1}{2}\mathrm{I} + \mathrm{K}_k - \mathrm{i}k\mathrm{V}_k)^{-1}(f_\Gamma \circ \mathbf{x}), \tag{3.6}$$

with I obviously being the identity operator. The above representation of the exterior scattered field, satisfying the SRC, provides an exact ansatz for the associated far-field as $(\mathcal{F}\varphi_{\rm per})(\widehat{\boldsymbol{z}})$, $\widehat{\boldsymbol{z}} \in \mathbb{S}^1$ defined, using the boundary density $\varphi_{\rm per} = (\frac{1}{2}\mathrm{I} + \mathrm{K}_k - \mathrm{i}k\mathrm{V}_k)^{-1}(f_\Gamma \circ \mathbf{x})$ [6]:

$$\left(\mathcal{F}\varphi_{\rm per}\right)(\widehat{\boldsymbol{z}}) := \sqrt{\frac{k}{8\pi}} \exp\left(-\tfrac{1}{4}\pi\mathrm{i}\right) \int_0^{2\pi} \exp(-\mathrm{i}k(\widehat{\boldsymbol{z}}\cdot\mathbf{x}(t)))\left[\widehat{\boldsymbol{z}}\cdot(x_2'(t), -x_1'(t)) + 1\right]\varphi_{\rm per}(t)\,\mathrm{d}t. \tag{3.7}$$

Thus accurate computational approximations of $\varphi_{\rm per}$ provide spectrally accurate approximations for both the scattered and the far-field. For computing $\varphi_{\rm per}$, the Nyström BEM solver makes use of a decomposition of the single- and double- layer operator into *logarithmic* and regular parts:

$$\begin{aligned}
(\mathrm{V}_k\varphi_{\rm per})(s) &= \int_0^{2\pi} A(s,t)\log\sin^2\tfrac{s-t}{2}\,\varphi_{\rm per}(t)\,\mathrm{d}t + \int_0^{2\pi} B(s,t)\varphi_{\rm per}(t)\,\mathrm{d}t,\\
(\mathrm{K}_k g_{\rm per})(s) &= \int_0^{2\pi} C(s,t)\log\sin^2\tfrac{s-t}{2}\,g_{\rm per}(t)\,\mathrm{d}t + \int_0^{2\pi} D(s,t)g_{\rm per}(t)\,\mathrm{d}t.
\end{aligned}$$

Functions $A,\ B,\ C,\ D$ are smooth and $2\pi-$biperiodic.

Next with N being a positive integer BEM discretization parameter, we consider the grid

$$\{t_j\}_{j\in\mathbb{Z}} \subset \mathbb{R}, \quad t_j := \tfrac{j\pi}{N},$$

and the $2N$-dimensional space of trigonometric polynomials defined by

$$\mathbb{T}_N := \mathrm{span}\langle e_\ell \ :\ \ell \in \mathbb{Z}_N\rangle, \quad e_\ell(t) := \exp(\mathrm{i}\ell t) \tag{3.8}$$

where $\mathbb{Z}_N = \{-N+1, -N+2, \ldots, N\}$. The interpolation operator for $2\pi-$periodic functions $\varphi_{\rm per}$

$$\mathbb{T}_N \ni \mathrm{Q}_N\varphi_{\rm per} \quad \text{s.t.} \quad (\mathrm{Q}_N\varphi_{\rm per})(t_j) = \varphi_{\rm per}(t_j),$$

is known to be well defined.

The Nyström method is based on the following approximations for the single- and double-layer operators:

$$\begin{aligned}
(\mathrm{V}_k^N\varphi_{\rm per})(s) &:= \int_0^{2\pi} \mathrm{Q}_N\big(A(s,\cdot)\varphi_{\rm per}\big)(t)\log\sin^2\tfrac{s-t}{2}\,\mathrm{d}t + \int_0^{2\pi} \mathrm{Q}_N\big(B(s,\cdot)\varphi_{\rm per}\big)(t)\,\mathrm{d}t\\
(\mathrm{K}_k^N g_{\rm per})(s) &:= \int_0^{2\pi} \mathrm{Q}_N\big(C(s,\cdot)g_{\rm per}\big)(t)\log\sin^2\tfrac{s-t}{2}\,\mathrm{d}t + \int_0^{2\pi} \mathrm{Q}_N\big(D(s,\cdot)g_{\rm per}\big)(t)\,\mathrm{d}t.
\end{aligned}$$

We stress that the integrals above can be computed exactly. Indeed,

$$-\frac{1}{2\pi}\int_0^{2\pi} \log\sin^2\tfrac{t}{2}\,e_n(t)\,\mathrm{d}t = -\frac{1}{2\pi}\int_0^{2\pi} \log\sin^2\tfrac{t}{2}\cos(nt)\,\mathrm{d}t = \begin{cases} \log 4, & n = 0\\ \frac{1}{|n|}, & n \neq 0, \end{cases}$$

and

$$\int_0^{2\pi} (\mathrm{Q}_N g_{\mathrm{per}})(t)\,\mathrm{d}t = \frac{\pi}{N}\sum_{j=0}^{2N-1} (\mathrm{Q}_N g_{\mathrm{per}})(t_j) = \frac{\pi}{N}\sum_{j=0}^{2N-1} g_{\mathrm{per}}(t_j),$$

i.e., for the regular part the suggested approximation yields the trapezoidal/rectangular rule for $2\pi-$periodic functions.

The evaluation of the potentials, as integral operators with smooth kernel, is carried out in a similar way:

$$\begin{aligned} \big(\mathrm{SL}_k^N \varphi_{\mathrm{per}}\big)(\boldsymbol{z}) &:= \int_0^{2\pi} \mathrm{Q}_N(\Phi_k(\boldsymbol{z}-\mathbf{x}(\cdot))\varphi_{\mathrm{per}})(t)\,\mathrm{d}t \\ \big(\mathrm{DL}_k^N g_{\mathrm{per}}\big)(\boldsymbol{z}) &:= \int_0^{2\pi} \mathrm{Q}_N\big(\big(\nabla_{\boldsymbol{y}}\Phi_k(\boldsymbol{z}-\boldsymbol{y})\big)\big|_{\boldsymbol{y}=\mathbf{x}(\cdot)} \cdot \boldsymbol{\nu}(\cdot)\, g_{\mathrm{per}}\big)(t)\,\mathrm{d}t. \end{aligned} \tag{3.9}$$

We are ready to present the discrete version for $\mathrm{K}^h_{\Omega_1^c\Gamma}$. Hence, in view of

$$\mathrm{K}_{\Omega_1^c\Gamma} f_\Gamma = (\mathrm{DL}_k - \mathrm{i}k\mathrm{SL}_k)\mathcal{L}_k(f_\Gamma\circ\mathbf{x}), \quad \text{with } \mathcal{L}_k := (\tfrac{1}{2}\mathrm{I} + \mathrm{K}_k - \mathrm{i}k\mathrm{V}_k)^{-1}, \tag{3.10}$$

we define for $f_{\mathrm{per}} := f_\Gamma\circ\mathbf{x}$

$$\mathrm{K}^N_{\Omega_1^c\Gamma} f_{\mathrm{per}} := (\mathrm{DL}_k^N - \mathrm{i}k\mathrm{SL}_k^N)\mathcal{L}_k^N f_{\mathrm{per}}, \quad \text{with } \mathcal{L}_k^N := (\tfrac{1}{2}\mathrm{I} + \mathrm{K}_k^N - \mathrm{i}k\mathrm{V}_k^N)^{-1}. \tag{3.11}$$

Hence $\varphi^N_{\mathrm{per}} := \mathcal{L}_k^N f_{\mathrm{per}}$ is the spectrally accurate approximation to the density $\varphi = \mathcal{L}_k f_\Gamma$. In addition, we can also introduce the associated far-field approximation, see (3.7), as

$$\big(\mathcal{F}_N\varphi^N_{\mathrm{per}}\big)(\widehat{\boldsymbol{z}}) := \sqrt{\frac{k}{8\pi}}\exp\big(-\tfrac{1}{4}\pi\mathrm{i}\big)\frac{\pi}{N}\sum_{j=-N+1}^{N} \exp(-\mathrm{i}k(\widehat{\boldsymbol{z}}\cdot\mathbf{x}(t_j)))\big[\widehat{\boldsymbol{z}}\cdot(x_2'(t_j),-x_1'(t_j))+1\big]\varphi^N_{\mathrm{per}}(t_j). \tag{3.12}$$

Remark 3.1. It is not difficult to show that

$$\varphi^N_{\mathrm{per}} = \mathcal{L}_k^N f_{\mathrm{per}} \quad \Rightarrow \quad \mathrm{Q}_N\varphi^N_{\mathrm{per}} = \mathrm{Q}_N\mathcal{L}_k^N\mathrm{Q}_N f_{\mathrm{per}}.$$

We note that only pointwise values of the density φ_{per} are used for computation of the BEM-based potentials and QoI. Accordingly, we can conclude that the true unknowns of the Nyström method are the values of the density at the grid points $\{\varphi_{\mathrm{per}}(t_j)\}_{j\in\mathbb{Z}}$ and that such values are computed by the algorithm using only the values of the right-hand-side f_{per} at the same grid.

The BEM-FEM coupling method

Let

$$\mathrm{K}^N_{\Sigma\Gamma} := \gamma_\Sigma \mathrm{K}^N_{\Omega_1^c\Gamma}, \quad \mathrm{K}^h_{\Gamma\Sigma} := (\gamma_\Gamma \mathrm{K}^h_{\Omega_2\Sigma})\circ\mathbf{x},$$

be the discrete counterparts of $\mathrm{K}_{\Sigma\Gamma}$ and $\mathrm{K}_{\Gamma\Sigma}$. That is, the first operator computes the BEM solution and evaluate on the outer polygonal domain Σ, whereas the second one solves the FEM problem and evaluates it on the interior and smooth Γ.

Then our coupled FEM-BEM algorithm is:

- Solve

$$(f_\Sigma^h, f_{\rm per}^N) \in \gamma_\Sigma \mathbb{P}_{h,d} \times \mathbb{T}_N \quad \text{s.t.}$$
$$\left(\mathcal{I} - \begin{bmatrix} & \mathrm{Q}_\Sigma^h \mathrm{K}_{\Sigma\Gamma}^N \\ \mathrm{Q}_N \mathrm{K}_{\Gamma\Sigma}^h & \end{bmatrix}\right) \begin{bmatrix} f_\Sigma^h \\ f_{\rm per}^N \end{bmatrix} = \begin{bmatrix} \mathrm{Q}_\Sigma^h \gamma_\Sigma u^{\rm inc} \\ -\mathrm{Q}_N \gamma_\Gamma (u^{\rm inc} \circ \mathbf{x}) \end{bmatrix}. \tag{3.13a}$$

- Construct

$$w_h = \mathrm{K}_{\Omega_2\Sigma}^h f_\Sigma^h, \quad \omega_N = \mathrm{K}_{\Omega_1^{\rm c}\Gamma}^N f_{\rm per}^N, \quad u_{h,N} = \begin{cases} w_h, & \text{in } \Omega_2, \\ \omega_N + u^{\rm inc}, & \text{in } \Omega_1^{\rm c}. \end{cases} \tag{3.13b}$$

Remark 3.2. In view of Remark 3.1, for implementation of the above algorithm, the pointwise values of the numerical solution $(f_\Sigma^h, f_{\rm per}^N)$ at the boundary nodes (of the FEM and BEM grids on Σ and Γ) are the true unknowns. Hence (3.13a) leads to a relatively small algebraic system.

We also note that, in view of the first-stage coupled and constrained solutions in (3.13a), the overlapped algorithm is designed in such a way that for sufficiently fine grids, the final-stage FEM and BEM parts of the algorithm in (3.13b) lead to two numerically coinciding solutions in $\Omega_{12} = \Omega_1^{\rm c} \cap \Omega_2$. (We demonstrate this property using numerical experiments.)

4 Numerical analysis of overlapped FEM-BEM algorithm

We analyze the above FEM-BEM scheme through rigorous derivation of the stability and convergence estimates in appropriate Sobolev norms. For the polygonal region we keep using the standard space $H^s(\Omega_1)$ and $H^s(\Sigma)$ (with the convention (2.5) for $s > 1$). For the smooth boundary Γ, since we switch to the parameterized spaced (via $\mathbf{x}$), we will work with $2\pi-$periodic Sobolev spaces. To this end, we define

$$H_{\rm per}^s := \{\varphi_{\rm per} \in \mathcal{D}'(\mathbb{R}) \ : \ \varphi_{\rm per} = \varphi_{\rm per}(\cdot + 2\pi), \ \|\varphi_{\rm per}\|_{H_{\rm per}^s} < \infty\}. \tag{4.1}$$

In (4.1), the distribution elements in the space are continuous linear functionals on $\mathcal{D}(\mathbb{R})$ (where $\mathcal{D}(\mathbb{R})$ is the space of the smooth compactly supported functions in $\mathbb{R}$ endowed with its natural topology), and the space is equipped with the norm

$$\|\varphi_{\rm per}\|_{H_{\rm per}^s}^2 = |\varphi_{\rm per}(0)|^2 + \sum_{n\neq 0} |n|^{2s} |\widehat{\varphi}_{\rm per}(n)|^2, \tag{4.2}$$

where $\widehat{\varphi}_{\rm per}(n)$ is the nth Fourier coefficient:

$$\widehat{\varphi}_{\rm per}(n) := \int_0^{2\pi} \varphi_{\rm per}(t) e_{-n}(t)\, \mathrm{d}t.$$

It is a well established result that $H^s(\Gamma)$ and $H_{\rm per}^s$ are isomorphic via the composition with $\mathbf{x}$ (see for example [28, Th. 8.13]).

4.1 Interpolation and some projection operators on the discrete spaces

For the implementation as well as for the theoretical analysis, we need some projections onto the discrete spaces defined on the boundaries Σ and Γ. In the first case we have already introduced the Lagrange interpolation operator in $\mathbb{P}_{h,d}$ (see (3.2)). For such operators it can be shown, as consequence of well-known results, that

$$\|\mathrm{Q}_\Sigma^h f_\Sigma - f_\Sigma\|_{H^s(\Sigma)} \leq C h_\Sigma^{t-s} \|f_\Sigma\|_{H^t(\Sigma)} \tag{4.3a}$$

where C depends only on Σ, $s \in [0,1]$ and $s \leq t < d+1$ and $t > 1/2$. Here and in what follows h_Σ is the maximum of the diameters of elements in Σ induced by the mesh $\mathcal{T}_h$. The convergence of order h_Σ^{d+1-s} can be attained if we assume an extra regularity for f_Σ: for any $s \in [0,1]$ and $t > d+1$, there exists C so that

$$\|\mathrm{Q}_\Sigma^h f_\Sigma - f_\Sigma\|_{H^s(\Sigma)} \leq C h_\Sigma^{d+1-s} \|f_\Sigma\|_{H^t(\Sigma)}. \tag{4.3b}$$

We refer the reader to Appendix A for proofs of such results. In this section we also introduce a more flexible projection on $\gamma_\Sigma \mathbb{P}_h^d$, which will be required for analysis purposes. Roughly speaking this is a consequence of carrying out the analysis in $H^1(\Omega)$ and $H^{1/2}(\Sigma)$ norms which, although are the natural ones for the FEM method, contains discontinuous functions and for which the action of Q_Σ^h cannot be therefore considered. Hence, we claim that there exists $\mathrm{P}_\Sigma^h : H^{1/2}(\Sigma) \to \gamma_\Sigma \mathbb{P}_{h,d}$ a projection on $\gamma_\Sigma \mathbb{P}_{h,d}$ satisfying

$$\|\mathrm{P}_\Sigma^h f_\Sigma - f_\Sigma\|_{H^s(\Sigma)} \leq C h_\Sigma^{t-s} \|f_\Sigma\|_{H^t(\Sigma)}, \quad 0 \leq s < 1, \quad s \leq t < d+1, \quad t \geq 1/2. \tag{4.4a}$$

$$\|\mathrm{P}_\Sigma^h f_\Sigma - f_\Sigma\|_{H^s(\Sigma)} \leq C h_\Sigma^{d+1-s} \|f_\Sigma\|_{H^t(\Sigma)}, \quad 0 \leq s < 1, \quad t > d+1. \tag{4.4b}$$

Proofs of the estimates (4.3) and (4.4) are given in Proposition A.1 and A.3 respectively in Appendix A.

The convergence of the trigonometric interpolation operator in the Sobolev frame is a well known result, see for example, [35, Th. 8.3.1]:

$$\|\mathrm{Q}_N \varphi_{\mathrm{per}} - \varphi_{\mathrm{per}}\|_{H^s_{\mathrm{per}}} \leq C N^{s-t} \|\varphi_{\mathrm{per}}\|_{H^t_{\mathrm{per}}}, \tag{4.5}$$

for any $t \geq s \geq 0$ and $t > 1/2$, where C depends only on s, t. For similar reasons, and again only for our analysis, we use the L^2-projection, which turns out to be the H^s-orthogonal projection for any s, on $\mathbb{T}_N$:

$$\mathbb{T}_N \ni \mathrm{P}_N \varphi_{\mathrm{per}}, \quad \text{s.t.} \quad \widehat{\mathrm{P}_N \varphi_{\mathrm{per}}}(n) = \widehat{\varphi_{\mathrm{per}}}(n), \quad n \in \mathbb{Z}_N.$$

It is straightforward to show that for any $t \geq s$,

$$\|\mathrm{P}_N \varphi_{\mathrm{per}} - \varphi_{\mathrm{per}}\|_{H^s_{\mathrm{per}}} \leq N^{s-t} \|\varphi_{\mathrm{per}}\|_{H^t_{\mathrm{per}}}. \tag{4.6}$$

With the help of these two projections we define

$$\mathcal{K}_{h,N} := \begin{bmatrix} & \mathrm{Q}_\Sigma^h \mathrm{K}_{\Sigma\Gamma}^N \mathrm{P}_N \\ \mathrm{Q}_N \mathrm{K}_{\Gamma\Sigma}^h \mathrm{P}_\Sigma^h & \end{bmatrix} \tag{4.7}$$

so that the (3.13a) can be set up as

$$(\mathcal{I} - \mathcal{K}_{h,N}) \begin{bmatrix} f_\Sigma \\ f_{\mathrm{per}} \end{bmatrix} = \begin{bmatrix} g_\Sigma \\ g_{\mathrm{per}} \end{bmatrix}$$

for appropriate $(g_\Sigma, g_{\rm per})^\top \in H^{1/2}(\Sigma)\times H^{1/2}_{\rm per}$. Observe that in the case that the right-hand-side $(g_\Sigma, g_{\rm per})$ belongs to the discrete space $\gamma_\Sigma\mathbb{P}_{h,d}\times\mathbb{T}_N$ (as in (3.13a)), so is the solution $(f_\Sigma, f_{\rm per})$. In this case, P^h_Σ and P_N in (4.7) are already acting on elements on the discrete space and can safely removed. Thus the role of these projections is to facilitate the analysis by setting up the equation in the continuous framework.

4.2 Convergence for the FEM scheme

We recall some classical convergence results as well as superconvergence phenomenon for the FEM solution in the following theorem.

Theorem 4.1. *For fixed $g_\Sigma \in H^{1/2}(\Sigma)$, $g^h_\Sigma \in \gamma_\Sigma\mathbb{P}_{h,d}$, let*

$$u := \mathrm{K}_{\Omega_2\Sigma} g_\Sigma, \quad u_h := \mathrm{K}^h_{\Omega_2\Sigma} g^h_\Sigma,$$

be the solution of the interior Helmholtz problem (2.6) and the approximation given by the FEM (3.1). Then there exists $C>0$ independent of g_Σ, g^h_Σ and h so that

$$\|u-u_h\|_{H^1(\Omega_2)} \le C\Big[\inf_{v_h\in\mathbb{P}_{h,d}} \|u-v_h\|_{H^1(\Omega_2)} + \|g_\Sigma - g^h_\Sigma\|_{H^{1/2}(\Sigma)}\Big]. \tag{4.8}$$

Furthermore, let D', D be domains with $D'\subset\overline{D}'\subset D\subset\overline{D}\subset\Omega_2\setminus\overline{\Omega_0}$ and $\{\mathcal{T}_h\}_h$ be a sequence of regular grids with $h\to 0$ which are quasi-uniform in D, that is

$$\min_{\substack{K\in\mathcal{T}_K\\ K\cap D\neq\emptyset}} h_K \ge c \max_{\substack{M\in\mathcal{T}_h\\ M\cap D\neq\emptyset}} h_M, \tag{4.9}$$

for some constant c independent of levels of discretization. Then there exists $\delta\in(1/2,1]$ such that for any $\varepsilon\in[0,1/2)$ and for any fine enough grid $\mathcal{T}_h$,

$$\|u-u_h\|_{H^{1+\varepsilon}(D')} \le C\big[(h^\delta h_D^{-\varepsilon}+h_D^{1-\varepsilon})\|u-u_h\|_{H^1(\Omega_2)} + h_D^{-\varepsilon}\|g_\Sigma-g^h_\Sigma\|_{L^2(\Sigma)} + h_D^{d-\varepsilon}\|u\|_{H^{d+1}(D)}\big] \tag{4.10}$$

with $C>0$ depending on ε, D and D', and h_D being the maximum of the diameters of the elements of the grid contained in D.

Proof. For (4.8) we refer to [37] (see also [11]). Estimate (4.10) can be derived using the superconvergence of the FEM solution in the interior of the computational domain where the solution is smooth (actually analytic) cf. [32]. We give a proof of these results in Corollary B.3 in Appendix B for the sake of completeness. □

Let us point out that the constant $\delta\in(1/2,1]$ in (4.10) depends on the regularity of the dual problem with homogeneous Dirichlet condition and a right-hand-side in $L^2(\Omega)$. Therefore, for convex polygonal domains in $\mathbb{R}^2$, we can take $\delta=1$ [20].

Assumption 1 Assume that for some open domain $D\subset\Omega_2\setminus\overline{\Omega}_0$ with $\Gamma\subset D$ there exists $\varepsilon_0>0$ such that the sequence of grids $\{\mathcal{T}_h\}_h$ is quasi-uniform in D and satisfies

$$h^{1/2}h_D^{-\varepsilon_0}\to 0$$

where h_D is the maximum of the diameters of the elements of the grid $\mathcal{T}_h$ having non-empty intersection with D. □

We note that this assumption allows locally refined grids but introduces a very weak restriction on the ratio between the larger element in Ω_2 and the smaller element in D. However, since the exact solution is smooth on D, it is reasonable to expect that small elements are not going to be used in this subdomain.

Lemma 4.2. *Let D and the sequence of grids $\{\mathcal{T}_h\}$ be as in Assumption 1. Then, for any open subset D' of D containing Γ and for any $\varepsilon \in [0, 1/2)$, there exists $C > 0$ such that*

$$\begin{aligned}&\|\mathrm{K}_{\Gamma\Sigma} f_\Sigma - \mathrm{K}^h_{\Gamma\Sigma}\mathrm{P}^h_\Sigma f_\Sigma\|_{H^{1/2+\varepsilon}_{\mathrm{per}}} \\ &\quad \le C h^{1/2} h_D^{-\varepsilon}\big[\inf_{v_h\in\mathbb{P}_{h,d}} \|\mathrm{K}_{\Omega_2\Sigma} f_\Sigma - v_h\|_{H^1(\Omega_2)} + \|f_\Sigma - \mathrm{P}^h_\Sigma f_\Sigma\|_{H^{1/2}(\Sigma)}\big] + C h_D^{d-\varepsilon}\|f_\Sigma\|_{L^2(\Sigma)}.\end{aligned}$$

Proof. Notice that

$$\|f_\Sigma - \mathrm{P}^h_\Sigma f_\Sigma\|_{L^2(\Sigma)} = \|f_\Sigma - \mathrm{P}^h_\Sigma f_\Sigma - \mathrm{P}^h_\Sigma(f_\Sigma - \mathrm{P}^h_\Sigma f_\Sigma)\|_{L^2(\Sigma)} \le C h^{1/2}\|f_\Sigma - \mathrm{P}^h_\Sigma f_\Sigma\|_{H^{1/2}(\Sigma)}.$$

Take D' so that $\Gamma \subset D' \subset \overline{D'} \subset D$. We claim that there exist C independent of f_Σ, so that

$$\|\mathrm{K}_{D\Sigma} f_\Sigma\|_{H^{d+1}(D)} \le C\|f_\Sigma\|_{L^2(\Sigma)}. \tag{4.11}$$

This can be seen as consequence of that the differential equations in D becomes the homogeneous Helmholtz equation and Γ is sufficiently far away from the boundary of D.

The continuity of the trace operator $\gamma_\Gamma : H^{1+\varepsilon}(D') \to H^{1/2+\varepsilon}(\Gamma) \sim H^{1/2+\varepsilon}_{\mathrm{per}}$ and a direct application of (4.8-4.10) yield

$$\begin{aligned}&\|\mathrm{K}_{\Gamma\Sigma} f_\Sigma - \mathrm{K}^h_{\Gamma\Sigma}\mathrm{P}^h_\Sigma f_\Sigma\|_{H^{1/2+\varepsilon}_{\mathrm{per}}} \\ &\quad \le C(h^\delta h_D^{-\varepsilon} + h_D^{1-\varepsilon} + h^{1/2-\varepsilon})\big[\inf_{v_h\in\mathbb{P}_{h,d}} \|\mathrm{K}_{\Omega_2\Sigma} f_\Sigma - v_h\|_{H^1(\Omega_2)} + \|f_\Sigma - \mathrm{P}^h_\Sigma f_\Sigma\|_{H^{1/2}(\Sigma)}\big] \\ &\qquad + C h_D^{d-\varepsilon}\|f_\Sigma\|_{L^2(\Sigma)}.\end{aligned}$$

Using that $\delta \ge 1/2$ the result is proven. □

We are ready to prove the convergence, in operator norm, of the first off diagonal block in (4.7) to the corresponding one in (2.10)

Proposition 4.3. *For any $0 < \varepsilon \le \varepsilon_0$ and for any $t \ge 0$ there exists $C > 0$ independent of f_Σ, h and N such that*

$$\begin{aligned}&\|\mathrm{K}_{\Gamma\Sigma} f_\Sigma - \mathrm{Q}_N\mathrm{K}^h_{\Gamma\Sigma}\mathrm{P}^h_\Sigma f_\Sigma\|_{H^{1/2}_{\mathrm{per}}} \\ &\quad \le C\big(1 + N^{-\varepsilon} h_D^{-\varepsilon}\big) h^{1/2}\big[\inf_{v_h\in\mathbb{P}_{h,d}} \|\mathrm{K}_{\Omega_2\Sigma} f_\Sigma - v_h\|_{H^1(\Omega_2)} + \|f_\Sigma - \mathrm{P}^h_\Sigma f_\Sigma\|_{H^{1/2}(\Sigma)}\big] \\ &\qquad + C(N^{-\varepsilon} h_D^{d-\varepsilon} + h_D^d + N^{-t})\|f_\Sigma\|_{L^2(\Sigma)}.\end{aligned} \tag{4.12}$$

In particular, we have the convergence in operator norm:

$$\|\mathrm{K}_{\Gamma\Sigma} - \mathrm{Q}_N\mathrm{K}^h_{\Gamma\Sigma}\mathrm{P}^h_\Sigma\|_{H^{1/2}(\Sigma)\to H^{1/2}_{\mathrm{per}}} \to 0 \quad \text{as } (N, h) \to (\infty, 0). \tag{4.13}$$

Proof. The identity

$$\mathrm{K}_{\Gamma\Sigma} - \mathrm{Q}_N \mathrm{K}^h_{\Gamma\Sigma} \mathrm{P}^h_\Sigma = \big(\mathrm{I} - \mathrm{Q}_N\big)\mathrm{K}_{\Gamma\Sigma} + (\mathrm{I} - \mathrm{Q}_N)\big(\mathrm{K}^h_{\Gamma\Sigma}\mathrm{P}^h_\Sigma - \mathrm{K}_{\Gamma\Sigma}\big) + \big(\mathrm{K}_{\Gamma\Sigma} - \mathrm{K}^h_{\Gamma\Sigma}\mathrm{P}^h_\Sigma\big), \tag{4.14}$$

and the estimates

$$\begin{aligned} \|(\mathrm{I} - \mathrm{Q}_N)\mathrm{K}_{\Gamma\Sigma} f_\Sigma\|_{H^{1/2}_{\mathrm{per}}} &\leq C N^{-t} \|\mathrm{K}_{\Gamma\Sigma} f_\Sigma\|_{H^{t+1/2}_{\mathrm{per}}} \leq C' N^{-t} \|f_\Sigma\|_{L^2(\Sigma)} \\ \|(\mathrm{I} - \mathrm{Q}_N)(\mathrm{K}^h_{\Gamma\Sigma}\mathrm{P}^h_\Sigma - \mathrm{K}_{\Gamma\Sigma}) f_\Sigma\|_{H^{1/2}_{\mathrm{per}}} &\leq C_{\varepsilon_1} N^{-\varepsilon_1} \|(\mathrm{K}^h_{\Gamma\Sigma}\mathrm{P}^h_\Sigma - \mathrm{K}_{\Gamma\Sigma}) f_\Sigma\|_{H^{1/2+\varepsilon_1}_{\mathrm{per}}}, \end{aligned}$$

which are consequences of (4.5) and (4.11), yield

$$\begin{aligned} &\|\mathrm{K}_{\Gamma\Sigma} f_\Sigma - \mathrm{Q}_N \mathrm{K}^h_{\Gamma\Sigma}\mathrm{P}^h_\Sigma f_\Sigma\|_{H^{1/2}_{\mathrm{per}}} \\ &\quad \leq C_\varepsilon N^{-\varepsilon_1} \|(\mathrm{K}^h_{\Gamma\Sigma}\mathrm{P}^h_\Sigma - \mathrm{K}_{\Gamma\Sigma}) f_\Sigma\|_{H^{1/2+\varepsilon_1}_{\mathrm{per}}} + C' N^{-t} \|f_\Sigma\|_{L^2(\Sigma)} + \|(\mathrm{K}^h_{\Gamma\Sigma}\mathrm{P}^h_\Sigma - \mathrm{K}_{\Gamma\Sigma}) f_\Sigma\|_{H^{1/2}_{\mathrm{per}}} \end{aligned}$$

Applying Lemma 4.2 twice (with $\varepsilon = \varepsilon_1$ for the first term and $\varepsilon = 0$ for the third one) yield (4.12). Consequently, (4.13) follows. □

4.3 Convergence for the BEM scheme

The inverse inequality

$$\|\varphi^N_{\mathrm{per}}\|_{H^t_{\mathrm{per}}} \leq N^{t-s} \|\varphi^N_{\mathrm{per}}\|_{H^s_{\mathrm{per}}}, \quad t \geq s, \quad \forall \varphi^N_{\mathrm{per}} \in \mathbb{T}_N, \tag{4.15}$$

that is straightforward to derive from (3.8) and (4.2), will be used repeatedly in this section. The first result in this subsection summarizes the convergence of the BEM solver in a format that will be used later. This is based on the convergence in norm of the approximation operator $\mathcal{L}^N_k$ to the continuous counterpart. We recall that $\mathcal{L}_k : H^s_{\mathrm{per}} \to H^s_{\mathrm{per}}$ is continuous for any $s \in \mathbb{R}$.

Theorem 4.4. *Fix $t \geq s > 1/2$. Then, there exists $C > 0$ such that for any N large enough and for any $f_{\mathrm{per}} \in H^t_{\mathrm{per}}$,*

$$\|\mathcal{L}_k f_{\mathrm{per}} - \mathcal{L}^N_k f_{\mathrm{per}}\|_{H^s_{\mathrm{per}}} \leq C N^{s-t-\alpha} \|f_{\mathrm{per}}\|_{H^t_{\mathrm{per}}}, \qquad \text{with } \alpha = \min\{s, 1\}. \tag{4.16}$$

Therefore, $\mathcal{L}^N_k : H^s_{\mathrm{per}} \to H^s_{\mathrm{per}}$ is uniformly continous in N for any $s > 1/2$.

Moreover, for $s, t \geq 0$, with $t \geq \max\{s-1, 0\}$ there exits $C > 0$ such that, for N large enough,

$$\|\mathrm{Q}_N \mathcal{L}_k \mathrm{P}_N f_{\mathrm{per}} - \mathrm{Q}_N \mathcal{L}^N_k \mathrm{P}_N f_{\mathrm{per}}\|_{H^s_{\mathrm{per}}} \leq C N^{s-t-\alpha} \|\mathrm{P}_N f_{\mathrm{per}}\|_{H^t_{\mathrm{per}}} \leq C N^{s-t-\alpha} \|f_{\mathrm{per}}\|_{H^t_{\mathrm{per}}}. \tag{4.17}$$

Proof. The estimates, recall (3.10) and (3.11),

$$\|\mathrm{K}^N_k - \mathrm{K}_k\|_{H^t_{\mathrm{per}} \to H^s_{\mathrm{per}}} + \|\mathrm{V}^N_k - \mathrm{V}_k\|_{H^t_{\mathrm{per}} \to H^s_{\mathrm{per}}} \leq C N^{s-t-\alpha}$$

with s, t, α as in the statement of the Theorem (see Chapter 12 and 13 in [28] or, for a more detailed proof, [12, Th. 3.1]) proves that $\mathcal{L}^N_k : H^s_{\mathrm{per}} \to H^s_{\mathrm{per}}$ for $s > 1/2$ is well defined, for N large enough, and it is uniformly bounded. Estimate (4.16) follows now from the identity

$$\mathcal{L}_k - \mathcal{L}^N_k = \mathcal{L}^N_k \big[(\mathcal{L}^N_k)^{-1} - \mathcal{L}^{-1}_k\big]\mathcal{L}_k = \mathcal{L}^N_k \big[(\mathrm{K}^N_k - \mathrm{K}_k) - \mathrm{i}k(\mathrm{V}^N_k - \mathrm{V}_k)\big]\mathcal{L}_k.$$

To prove the second estimate (4.17), we proceed in two steps: For $s \in [1,\infty)$, $t \geq s-1$ we have

$$\begin{aligned}\|\mathrm{Q}_N\mathcal{L}_k^N\mathrm{P}_N f_{\mathrm{per}} - \mathrm{Q}_N\mathcal{L}_k\mathrm{P}_N f_{\mathrm{per}}\|_{H^s_{\mathrm{per}}} &\leq C\|(\mathcal{L}_k^N - \mathcal{L}_k)\mathrm{P}_N f_{\mathrm{per}}\|_{H^s_{\mathrm{per}}} \leq C' N^{s-t-2}\|\mathrm{P}_N f_{\mathrm{per}}\|_{H^{t+1}_{\mathrm{per}}} \\ &\leq C' N^{s-t-1}\|\mathrm{P}_N f_{\mathrm{per}}\|_{H^t_{\mathrm{per}}}. \end{aligned} \tag{4.18}$$

(Notice that in the last step we have used the inverse inequality (4.15).) On the other hand, for $s \in [0,1]$ and $t \geq 0$, we make use of the bound $\|\mathrm{Q}_N g_{\mathrm{per}}\|_{H^0_{\mathrm{per}}} \leq C\|g_{\mathrm{per}}\|_{H^1_{\mathrm{per}}}$ to derive

$$\begin{aligned}\|\mathrm{Q}_N\mathcal{L}_k^N\mathrm{P}_N f_{\mathrm{per}} - \mathrm{Q}_N\mathcal{L}_k\mathrm{P}_N f_{\mathrm{per}}\|_{H^s_{\mathrm{per}}} &\leq C\|(\mathcal{L}_k^N - \mathcal{L}_k)\mathrm{P}_N f_{\mathrm{per}}\|_{H^1_{\mathrm{per}}} \leq C' N^{-t-1}\|\mathrm{P}_N f_{\mathrm{per}}\|_{H^{t+1}_{\mathrm{per}}} \\ &\leq C' N^{-t}\|\mathrm{P}_N f_{\mathrm{per}}\|_{H^t_{\mathrm{per}}}. \end{aligned} \tag{4.19}$$

Estimates (4.18) and (4.19) yield the desired result (4.17). □

Lemma 4.5. *For any domain D with $\overline{D} \cap \Gamma = \emptyset$ and any r, s there exists $C > 0$ such that for any N and $\varphi^N_{\mathrm{per}} \in \mathbb{T}_N$,*

$$\|\mathrm{DL}_k^N\varphi^N_{\mathrm{per}} - \mathrm{DL}_k\varphi^N_{\mathrm{per}}\|_{H^s(D)} + \|\mathrm{SL}_k^N\varphi^N_{\mathrm{per}} - \mathrm{SL}_k\varphi^N_{\mathrm{per}}\|_{H^s(D)} \leq CN^{-r}\|\varphi^N_{\mathrm{per}}\|_{H^0_{\mathrm{per}}}. \tag{4.20}$$

Proof. Since the kernels of the integral operators are smooth, the estimate follows from the aliasing effect of the trapezoidal rule for periodic functions. Indeed, for $|n| \leq N$ we have for any g smooth enough

$$\left|\frac{\pi}{N}\sum_{j=0}^{2N-1} g_{\mathrm{per}}(t_j)e_{-n}(t_j) - \int_0^{2\pi} g_{\mathrm{per}}(t)e_{-n}(t)\,\mathrm{d}t\right| \leq \frac{1}{2\pi}\sum_{\ell\neq 0}|\widehat{g}_{\mathrm{per}}(n+2\ell N)|, \quad e_n(t) := \exp(\mathrm{i}nt)$$

(see for instance [28, 35]). Hence, for any $\varphi^N_{\mathrm{per}} \in \mathbb{T}_N$

$$\left|\frac{\pi}{N}\sum_{j=0}^{2N-1} g_{\mathrm{per}}(t_j)\varphi^N_{\mathrm{per}}(t_j) - \int_0^{2\pi} g_{\mathrm{per}}(t)\varphi^N_{\mathrm{per}}(t)\,\mathrm{d}t\right| \leq \frac{1}{2\pi}\sum_{n\in\mathbb{Z}_N}|\widehat{\varphi}_{\mathrm{per}}(n)|\sum_{\ell\neq 0}|\widehat{g}_{\mathrm{per}}(-n+2\ell N)|.$$

The last term can be easily bounded using the Cauchy-Schwarz inequality:

$$\begin{aligned}\sum_{n\in\mathbb{Z}_N}|\varphi^N_{\mathrm{per}}(n)|\sum_{\ell\neq 0}|\widehat{g}_{\mathrm{per}}(-n+2\ell N)| &\leq (2N)^{-r}\|\varphi^N_{\mathrm{per}}\|_{H^0_{\mathrm{per}}}\Bigg[\sum_{n\in\mathbb{Z}_N}\underbrace{\left(\sum_{\ell\neq 0}\frac{1}{|\ell - n/(2N)|^{2r}}\right)}_{=:C_r(n/(2N))} \\ &\qquad \times\left(\sum_{\ell\neq 0}|-n+2\ell N|^{2r}|\widehat{g}_{\mathrm{per}}(-n+2\ell N)|^2\right)\Bigg]^{1/2} \\ &\leq C_r N^{-r}\|\varphi^N_{\mathrm{per}}\|_{H^0_{\mathrm{per}}}\|g_{\mathrm{per}}\|_{H^r_{\mathrm{per}}}\end{aligned}$$

which is valid for any $r > 1/2$. (We have used above that the series function $C_r(z)$ is bounded for $|z| \leq 1/2$) □

Corollary 4.6. *For any $s \geq 0$, there exists $C > 0$ so that for any N,*

$$\|\mathrm{Q}_N\mathcal{L}_k^N\mathrm{P}_N f_{\mathrm{per}}\|_{H^s_{\mathrm{per}}} \leq C\|\mathrm{P}_N f_{\mathrm{per}}\|_{H^s_{\mathrm{per}}} \leq C\|f_{\mathrm{per}}\|_{H^s_{\mathrm{per}}}.$$

Proof. The identity

$$\mathcal{L}_k = 2\mathrm{I} - \mathrm{M}_k, \quad \mathrm{M}_k := 2\mathcal{L}_k(\mathcal{L}_k^{-1} - \tfrac{1}{2}\mathrm{I}) = 2\mathcal{L}_k(\mathrm{K}_k - \mathrm{i}k\mathrm{V}_k) \tag{4.21}$$

and the mapping properties $\mathrm{V}_k - \mathrm{i}k\mathrm{K}_k : H^s_{\mathrm{per}} \to H^{s+1}_{\mathrm{per}}$ (see for instance, [35, Section 6.2]) yield

$$\begin{aligned} \|\mathrm{Q}_N\mathcal{L}_k\mathrm{P}_N f_{\mathrm{per}} - \mathcal{L}_k\mathrm{P}_N f_{\mathrm{per}}\|_{H^s_{\mathrm{per}}} &= \|\mathrm{Q}_N\mathrm{M}_k\mathrm{P}_N f_{\mathrm{per}} - \mathrm{M}_k\mathrm{P}_N f_{\mathrm{per}}\|_{H^s_{\mathrm{per}}} \\ &\le C'N^{-1}\|\mathrm{M}_k\mathrm{P}_N f_{\mathrm{per}}\|_{H^{s+1}_{\mathrm{per}}} \le CN^{-1}\|f_{\mathrm{per}}\|_{H^s_{\mathrm{per}}} \end{aligned} \tag{4.22}$$

where we have used also (4.5) and (4.6). The result follows readily from the decomposition

$$\begin{aligned} \|\mathrm{Q}_N\mathcal{L}_k^N\mathrm{P}_N f_{\mathrm{per}}\|_{H^s_{\mathrm{per}}} \le\ & \|\mathcal{L}_k\mathrm{P}_N f_{\mathrm{per}}\|_{H^s_{\mathrm{per}}} + \|\mathrm{Q}_N\mathcal{L}_k^N\mathrm{P}_N f_{\mathrm{per}} - \mathrm{Q}_N\mathcal{L}_k\mathrm{P}_N f_{\mathrm{per}}\|_{H^s_{\mathrm{per}}} \\ & + \|\mathrm{Q}_N\mathcal{L}_k\mathrm{P}_N f_{\mathrm{per}} - \mathcal{L}_k\mathrm{P}_N f_{\mathrm{per}}\|_{H^s_{\mathrm{per}}}, \end{aligned}$$

and the estimates (4.22) and (4.17) in Theorem 4.4. □

We are ready to prove the convergence of the corresponding block in (4.7).

Proposition 4.7. *For any $t \ge 0$, there exists $C > 0$ such that for any h, N and $f_{\mathrm{per}} \in H^t_{\mathrm{per}}$,*

$$\|\mathrm{K}_{\Sigma\Gamma} f_{\mathrm{per}} - \mathrm{Q}^h_\Sigma \mathrm{K}^N_{\Sigma\Gamma}\mathrm{P}_N f_{\mathrm{per}}\|_{H^{1/2}(\Sigma)} \le C(N^{-t}\|f_{\mathrm{per}}\|_{H^t_{\mathrm{per}}} + h_\Sigma^{d+1/2}\|f_{\mathrm{per}}\|_{H^0_{\mathrm{per}}}). \tag{4.23}$$

In particular, we have the convergence in operator norm:

$$\|\mathrm{K}_{\Sigma\Gamma} f_{\mathrm{per}} - \mathrm{Q}^h_\Sigma \mathrm{K}^N_{\Sigma\Gamma}\mathrm{P}_N f_{\mathrm{per}}\|_{H^{1/2}_{\mathrm{per}} \to H^{1/2}(\Sigma)} \to 0 \quad \textit{as } (N, h) \to (\infty, 0). \tag{4.24}$$

Proof. For the purpose of this proof, we define

$$\mathrm{R}_{\Sigma\Gamma} := \gamma_\Sigma(\mathrm{DL}_k - \mathrm{i}k\mathrm{SL}_k), \quad \mathrm{R}^N_{\Sigma\Gamma} := \gamma_\Sigma(\mathrm{DL}^N_k - \mathrm{i}k\mathrm{SL}^N_k). \tag{4.25}$$

Clearly $\mathrm{R}_{\Sigma\Gamma} : H^0_{\mathrm{per}} \to H^t(\Sigma)$ is continuous, for any t, and, from Lemma 4.5, (see also (3.10))

$$\|\mathrm{R}_{\Sigma\Gamma}\mathrm{Q}_N\varphi_{\mathrm{per}} - \mathrm{R}^N_{\Sigma\Gamma}\mathrm{Q}_N\varphi_{\mathrm{per}}\|_{H^m(\Sigma)} \le C_t N^{-t}\|\mathrm{Q}_N\varphi_{\mathrm{per}}\|_{H^0_{\mathrm{per}}} \tag{4.26}$$

for any t and m, with C independent of φ_{per} and N. We also have for any compact domain D far away from Γ and for any $t \ge 0$,

$$\|\mathrm{R}_{\Sigma\Gamma}\varphi_{\mathrm{per}}\|_{H^m(D)} \le C\|\varphi_{\mathrm{per}}\|_{H^{-t}_{\mathrm{per}}} \tag{4.27}$$

which in particular implies cf. (4.3b)

$$\|(\mathrm{I} - \mathrm{Q}^h_\Sigma)\mathrm{R}_{\Sigma\Gamma}\varphi_{\mathrm{per}}\|_{H^{1/2}(\Sigma)} \le Ch_\Sigma^{d+1/2}\|\varphi_{\mathrm{per}}\|_{H^{-t}_{\mathrm{per}}}, \qquad \|\mathrm{Q}^h_\Sigma\mathrm{R}_{\Sigma\Gamma}\varphi_{\mathrm{per}}\|_{H^{1/2}(\Sigma)} \le C\|\varphi_{\mathrm{per}}\|_{H^{-t}_{\mathrm{per}}}. \tag{4.28}$$

Write now

$$\begin{aligned} \mathrm{K}_{\Sigma\Gamma} - \mathrm{Q}^h_\Sigma\mathrm{K}^N_{\Sigma\Gamma}\mathrm{P}_N &= \mathrm{R}_{\Sigma\Gamma}\mathcal{L}_k - \mathrm{Q}^h_\Sigma\mathrm{R}^N_{\Sigma\Gamma}\mathrm{Q}_N\mathcal{L}^N_k\mathrm{P}_N \\ &= (\mathrm{I} - \mathrm{Q}^h_\Sigma)\mathrm{R}_{\Sigma\Gamma}\mathcal{L}_k + \mathrm{Q}^h_\Sigma\mathrm{R}_{\Sigma\Gamma}\mathcal{L}_k(\mathrm{I} - \mathrm{P}_N) \\ &\quad + \mathrm{Q}^h_\Sigma\mathrm{R}_{\Sigma\Gamma}(\mathrm{I} - \mathrm{Q}_N)\mathcal{L}_k\mathrm{P}_N + \mathrm{Q}^h_\Sigma\mathrm{R}_{\Sigma\Gamma}(\mathrm{Q}_N\mathcal{L}_k - \mathrm{Q}_N\mathcal{L}^N_k)\mathrm{P}_N \\ &\quad + \mathrm{Q}^h_\Sigma(\mathrm{R}_{\Sigma\Gamma} - \mathrm{R}^N_{\Sigma\Gamma})\mathrm{Q}_N\mathcal{L}^N_k\mathrm{P}_N \\ &=: \mathrm{L}^h_1 + \mathrm{L}^{h,N}_2 + \mathrm{L}^{h,N}_3 + \mathrm{L}^{h,N}_4 + \mathrm{L}^{h,N}_5. \end{aligned} \tag{4.29}$$

Let us bound these terms now. From (4.28) and the continuity $\mathcal{L}_k : H^s_{\rm per} \to H^s_{\rm per}$,

$$\|\mathrm{L}_1^h f_{\rm per}\|_{H^{1/2}(\Sigma)} \le C h_\Sigma^{d+1/2} \|\mathcal{L}_k f_{\rm per}\|_{H^0_{\rm per}} \le C' h_\Sigma^{d+1/2} \|f_{\rm per}\|_{H^0_{\rm per}}.$$

Proceeding similarly we derive from (4.6),

$$\|\mathrm{L}_2^{h,N} f_{\rm per}\|_{H^{1/2}(\Sigma)} \le C \|(\mathrm{I} - \mathrm{P}_N) f_{\rm per}\|_{H^{-t}_{\rm per}} \le C N^{-t} \|f_{\rm per}\|_{H^0_{\rm per}},$$

and, by (4.5),

$$\|\mathrm{L}_3^{h,N} f_{\rm per}\|_{H^{1/2}(\Sigma)} \le C \|(\mathrm{I} - \mathrm{Q}_N)\mathcal{L}_k \mathrm{P}_N f_{\rm per}\|_{H^0_{\rm per}} \le C'' N^{-t} \|f_{\rm per}\|_{H^t_{\rm per}}.$$

The fourth term is bounded using (4.17) in Theorem 4.4,

$$\|\mathrm{L}_4^{h,N} f_{\rm per}\|_{H^{1/2}(\Sigma)} \le C \|(\mathrm{Q}_N \mathcal{L}_k \mathrm{P}_N - \mathrm{Q}_N \mathcal{L}_k^N \mathrm{P}_N) f_{\rm per}\|_{H^0_{\rm per}} \le C'' N^{-t} \|f_{\rm per}\|_{H^t_{\rm per}}.$$

Finally, (4.28) again, (4.26) with Corollary 4.6 yield,

$$\|\mathrm{L}_5^{h,N} f_{\rm per}\|_{H^{1/2}(\Sigma)} \le C N^{-t} \|\mathrm{Q}_N \mathcal{L}_k^N \mathrm{P}_N f_{\rm per}\|_{H^0_{\rm per}} \le C N^{-t} \|f_{\rm per}\|_{H^0_{\rm per}}.$$

Gathering these bounds yields the estimate (4.23), and consequently (4.24) holds.

□

4.4 Convergence of the full scheme

We are ready to prove the main result of this paper: stability and convergence for the FEM-BEM numerical algorithm.

Theorem 4.8. *For any N large enough and $\mathcal{T}_h$ sufficiently fine satisfying Assumption 1, the mapping*

$$\mathcal{I} - \mathcal{K}_{h,N} : H^{1/2}(\Sigma) \times H^{1/2}_{\rm per} \to H^{1/2}(\Sigma) \times H^{1/2}_{\rm per}$$

is uniformly bounded, invertible and with inverse uniformly bounded.

Moreover, if (f_Σ, f_Γ) is the solution of (2.9a) and $(f_\Sigma^h, f_{\rm per}^N)$ that of (3.13a), then for any $r \ge 0$ and $0 < \varepsilon \le \varepsilon_0$, with ε_0 as in Assumption 1, we have the following estimate, with $f_{\rm per} = f_\Gamma \circ \mathbf{x}$,

$$\begin{aligned}
&\|f_\Sigma - f_\Sigma^h\|_{H^{1/2}(\Sigma)} + \|f_{\rm per} - f_{\rm per}^N\|_{H^{1/2}_{\rm per}} \\
&\quad \le C \Big[\|\gamma_\Sigma u^{\rm inc} - \mathrm{Q}_\Sigma^h \gamma_\Sigma u^{\rm inc}\|_{H^{1/2}(\Sigma)} + \|u^{\rm inc} \circ \mathbf{x} - \mathrm{Q}_N u^{\rm inc} \circ \mathbf{x}\|_{H^{1/2}_{\rm per}} \\
&\qquad + \big(h_D^{-\varepsilon} N^{-\varepsilon} + 1\big) h^{1/2} \big[\inf_{v_h \in \mathbb{P}_{h,d}} \|\mathrm{K}_{\Omega_2\Sigma} f_\Sigma - v_h\|_{H^1(\Omega_2)} + \|f_\Sigma - \mathrm{P}_\Sigma^h f_\Sigma\|_{H^{1/2}(\Sigma)} \big] \\
&\qquad + (N^{-\varepsilon} h_D^{d-\varepsilon} + h_D^d + N^{-r}) \|f_\Sigma\|_{L^2(\Sigma)} + (N^{-t} + h_\Sigma^{d+1/2}) \|f_{\rm per}\|_{H^t_{\rm per}} \Big]
\end{aligned} \tag{4.30}$$

with C independent of f_Σ, $f_{\rm per}$, h and N.

Proof. From (4.13) and (4.24) in Propositions 4.3 and 4.7 we conclude

$$\|\mathcal{K} - \mathcal{K}_{h,N}\|_{H^{1/2}(\Sigma) \times H^{1/2}_{\rm per} \to H^{1/2}(\Sigma) \times H^{1/2}_{\rm per}} \to 0, \quad \text{as } (h, N) \to (0, \infty)$$

which proves the first part of the theorem.

On the other hand, for small enough $c > 0$, independent of h and N, it holds

$$\begin{aligned} c\big(\|f_\Sigma - f_\Sigma^h\|_{H^{1/2}(\Sigma)} + \|f_{\rm per} - f_{\rm per}^N\|_{H^{1/2}_{\rm per}}\big) \;&\le\; \left\|(\mathcal{I} - \mathcal{K}_{h,N}) \begin{bmatrix} f_\Sigma - f_\Sigma^h \\ f_{\rm per} - f_{\rm per}^N \end{bmatrix}\right\|_{H^{1/2}(\Sigma)\times H^{1/2}_{\rm per}} \\ &\le \left\| \begin{bmatrix} \gamma_\Sigma u^{\rm inc} - \mathrm{Q}_\Sigma^h \gamma_\Sigma u^{\rm inc} \\ u^{\rm inc}\circ\mathbf{x} - \mathrm{Q}_N u^{\rm inc}\circ\mathbf{x} \end{bmatrix}\right\|_{H^{1/2}(\Sigma)\times H^{1/2}_{\rm per}} \\ &\quad + \left\|(\mathcal{K} - \mathcal{K}_{h,N}) \begin{bmatrix} f_\Sigma \\ f_{\rm per} \end{bmatrix}\right\|_{H^{1/2}(\Sigma)\times H^{1/2}_{\rm per}} \end{aligned} \tag{4.31}$$

and the estimate (4.30) follows from Propositions 4.3 and 4.7. □

Theorem 4.9. *Let $(u,\omega) = (\mathrm{K}_{\Omega_2\Sigma} f_\Sigma, \mathrm{K}_{\Omega_1^c\Gamma} f_\Gamma)$ be the exact solution of (2.9), and let $(u_h,\omega_N) := (\mathrm{K}^h_{\Omega_2\Sigma} f_\Sigma^h, \mathrm{K}^N_{\Omega_1^c\Gamma} f_{\rm per}^N)$ be that of the FEM-BEM system (3.13). Then, for any compact set $D \subset \mathbb{R}^d \setminus \overline{\Omega}_1$, $r \ge 0$, $t > d + 1/2$ there exist C such that*

$$\begin{aligned} &\|u - u_h\|_{H^1(\Omega_2)} + \|\omega - \omega_N\|_{H^r(D)} \\ &\quad\le\; C\big(h_D^{d-\varepsilon} N^{-\varepsilon} + h_\Sigma^{d+1/2} + N^{-t} + h_D^d\big)\|u^{\rm inc}\|_{H^{t+1}(\Omega_2)} + C \inf_{v_h\in\mathbb{P}_{h,d}} \|u - v_h\|_{H^1(\Omega_2)}. \end{aligned} \tag{4.32}$$

Proof. Notice that as consequence of Theorem 2.1, and with $f_{\rm per} = f\circ\mathbf{x}$ as before,

$$\|f_\Sigma\|_{H^{t+1/2}(\Sigma)} + \|f_{\rm per}\|_{H^{t+1/2}_{\rm per}} \le C_t \|u^{\rm inc}\|_{H^{t+1}(\Omega_2)},$$

and, cf. (4.3) and (4.5),

$$\begin{aligned} \|\gamma_\Sigma u^{\rm inc} - \mathrm{Q}_\Sigma^h \gamma_\Sigma u^{\rm inc}\|_{H^{1/2}(\Sigma)} \;&\le\; C h_\Sigma^{d+1/2} \|u^{\rm inc}\|_{H^{t+1}(\Omega_2)}, \\ \|u^{\rm inc}\circ\mathbf{x} - \mathrm{Q}_N u^{\rm inc}\circ\mathbf{x}\|_{H^{1/2}_{\rm per}} \;&\le\; C N^{-t} \|u^{\rm inc}\|_{H^{t+1}(\Omega_2)}. \end{aligned}$$

Since

$$\|f_\Sigma - \mathrm{P}_\Sigma^h f_\Sigma\|_{H^{1/2}(\Sigma)} \le C' \inf_{p_h\in\gamma_\Sigma\mathbb{P}_{h,d}} \|f_\Sigma - p_h\|_{H^{1/2}(\Sigma)} \le C' \|f_\Sigma - f_\Sigma^h\|_{H^{1/2}(\Sigma)},$$

the estimate (4.30) yields

$$\begin{aligned} \|f_\Sigma - f_\Sigma^h\|_{H^{1/2}(\Sigma)} + \|f_{\rm per} - f_{\rm per}^N\|_{H^{1/2}_{\rm per}} \;&\le\; c(h,N)\|f_\Sigma - f_\Sigma^h\|_{H^{1/2}(\Sigma)} \\ &\quad + C\big(h_D^{d-\varepsilon} N^{-\varepsilon} + h_D^d + N^{-t} + h_\Sigma^{d+1/2}\big)\|u^{\rm inc}\|_{H^{t+1}(\Omega_2)} \\ &\quad + C' \inf_{v_h\in\mathbb{P}_{h,d}} \|u - v_h\|_{H^1(\Omega_2)}. \end{aligned} \tag{4.33}$$

with $c(h,N) \to 0$ as $(h,N) \to (0,\infty)$. (Actually C' above can be shown to tend to zero as $(h,N)\to(0,\infty)$). Taking h sufficiently small and N large enough, say such that $c(h,N) < 1/2$, the estimate for the error $u - u_h$ follows from (4.8) in Theorem 4.1.

Regarding the other term, we notice that by Lemma 4.5

$$\begin{aligned} \|\omega - \omega_N\|_{H^r(D)} \;&=\; \|(\mathrm{DL}_k - \mathrm{i}k\mathrm{SL}_k)\mathcal{L}_k f_{\rm per} - (\mathrm{DL}_k^N - \mathrm{i}k\mathrm{SL}_k^N)\mathrm{Q}_N\mathcal{L}_k^N f_{\rm per}^N\|_{H^r(D)} \\ &\le\; C\left(\|\mathcal{L}_k f_{\rm per} - \mathrm{Q}_N\mathcal{L}_k f_{\rm per}\|_{H^0_{\rm per}} + \|\mathrm{Q}_N\mathcal{L}_k f_{\rm per} - \mathrm{Q}_N\mathcal{L}_k^N f_{\rm per}^N\|_{H^0_{\rm per}}\right). \end{aligned} \tag{4.34}$$

Recalling that M_k in (4.21) is a pseudo-differential operator of order -1, we obtain the bound

$$\|\mathcal{L}_k f_{\rm per} - \mathrm{Q}_N \mathcal{L}_k f_{\rm per}\|_{H^0_{\rm per}} = \|(\mathrm{I} - \mathrm{Q}_N)\mathrm{M}_k f_{\rm per}\|_{H^0_{\rm per}} \leq C N^{-t-3/2} \|f_{\rm per}\|_{H^{t+1/2}_{\rm per}}.$$

Next, we claim that for the second term in (4.34) the following bound holds

$$\|\mathrm{Q}_N \mathcal{L}_k f_{\rm per} - \mathrm{Q}_N \mathcal{L}_k^N f_{\rm per}^N\|_{H^0_{\rm per}} \leq C \| \mathrm{P}_N f_{\rm per} - f_{\rm per}^N\|_{H^{1/2}_{\rm per}} + N^{-t-1/2} \|f_{\rm per}\|_{H^{t+1/2}_{\rm per}} \tag{4.35}$$

which, with estimate (4.33), should prove the result. Indeed, writing

$$\begin{aligned} &\mathrm{Q}_N \mathcal{L}_k f_{\rm per} - \mathrm{Q}_N \mathcal{L}_k^N f_{\rm per}^N \\ &\qquad = \mathrm{Q}_N \mathcal{L}_k (f_{\rm per} - \mathrm{P}_N f_{\rm per}) + (\mathrm{Q}_N \mathcal{L}_k \mathrm{P}_N f_{\rm per} - \mathrm{Q}_N \mathcal{L}_k^N \mathrm{P}_N f_{\rm per}) + \mathrm{Q}_N \mathcal{L}_k^N (\mathrm{P}_N f_{\rm per} - f_{\rm per}^N), \end{aligned}$$

and using

$$\begin{aligned} \|\mathrm{Q}_N \mathcal{L}_k (f_{\rm per} - \mathrm{P}_N f_{\rm per})\|_{H^0_{\rm per}} &\leq \|\mathcal{L}_k (f_{\rm per} - \mathrm{P}_N f_{\rm per})\|_{H^0_{\rm per}} + C N^{-1} \|\mathcal{L}_k (f_{\rm per} - \mathrm{P}_N f_{\rm per})\|_{H^1_{\rm per}} \\ &\leq C' N^{-t-1/2} \|f_{\rm per}\|_{H^{t+1/2}_{\rm per}} \end{aligned}$$

for the first term, (4.17) in Theorem 4.4 (with $s = \alpha = 0$) for the second one and Corollary 4.6 for the third term, (4.35) follows. □

5 Numerical experiments

This section comprises three sets of numerical experiments to demonstrate our FEM-BEM algorithm and analysis. As proved in Theorem 4.9, convergence of the FEM-BEM numerical solution is dictated by the best approximation last term in (4.32). The best approximation accuracy depends on the smoothness of the exact solution u of (2.1), induced by smoothness of the refractive index n in the heterogeneous region.

The first set of experiments is for the smooth solution case to observe the fast convergence of our method under optimal conditions. Motivation for the second and third set of experimstents are from the Janus particle configurations with non-smooth (only piecewise-continuous) refractive indices. For the second and third experiments, the total wave has limited regularity and belongs to $H^2(\Omega_2) \setminus H^{5/2}(\Omega)$. (The *discontinuity* of the refractive index n in Ω_2 leads to the interior wave-field limitation that $\Delta u \notin H^{1/2}(\Omega_2)$.) For the latter cases, we also demonstrate that our FEM-BEM algorithm converges, with lower convergence rates, and good accuracy can be obtained using high-order finite elements (such as the FEM space spanned by quadratic or cubic splines). In particular for the multi-particle Janus-type configuration experiments, we demonstrate that even quadratic FEM is not sufficient, highlighting the difficulty associated with Janus configurations for wave propagation models and the need for efficient high-order FEM-BEM to compute approximations for the practical QoI such as the DSCS and OA-DSCS. We recall that these QoI are defined in (2.4) and in the algorithm, the far-field is computed using the density based ansatz in (3.12).

Basic setup of the three sets of experiments is similar. Starting from an initial, coarse mesh $\mathcal{T}_H$, we consider a set of meshes $\mathcal{T}_H \subset \mathcal{T}_{H/2} \subset \cdots \mathcal{T}_h \subset \mathcal{T}_{h/2} \subset \cdots \mathcal{T}_{h_e}$ obtained from successive uniform refinement where each triangle is divided into four elements. For the BEM solver we proceed analogously, consider an initial, relatively low number $N = N_0$, and then we double the points: $\{N_0, 2N_0, \ldots, N_e\}$.

One of aims of the numerical experiments is to demonstrate the error estimates proved in Theorem 4.9. This is carried out as follows: Let $\mathcal{T}_{h_e}$ be the finest of the chosen finite element grids and let N_e be the largest of the chosen BEM discrete parameters. We then compute the solution $(u_{h_e/2}, \omega_{2N_e})$ using next refinement steps. We will use this pair as our reference exact solution, i.e. with the notation of Theorem 4.9, $(u_{h_e/2}, \omega_{2N_e}) \approx (u, \omega)$ so that we compute

$$\|u_h - u_{h_e/2}\|_{H^1(\Omega_2)}; \qquad \|\mathrm{Q}_{h_e/2}(\omega_N - \omega_{2N_e})\|_{H^1(D)}, \tag{5.1}$$

as the H^1-error for the finite element solution (total wave) and boundary element solution (scattered wave). Here, $\mathrm{Q}_{h_e/2}$ is the Lagrange interpolation operator on $\mathbb{P}_{h_e/2,d}$ which means $\mathrm{Q}_{h_e/2}u_{h_e/2} = u_{h_e/2}$ and $\mathrm{Q}_{h_e/2}u_h = u_h$ for any u_h in our list of experiments. Since both ω_N and ω are smooth functions as long as $\overline{D} \subset \mathrm{ext}(\Gamma)$ (the region exterior to Γ), such a strategy gives a sufficiently good estimate for the true error of the numerical solution.

In our computations we have taken D in (5.1) to be $\mathcal{T}_{h_e/2} \cap \mathrm{Ext}(r\Gamma) \cap \Omega_2$, with $r = 1.1$ to ensure no instabilities for evaluation of potentials in (3.11). Mesh generation in our experiments were obtained using the open-source package GMSH [18], that is efficient for generation of triangular meshes on complex geometries Ω_0. Our choice of a complex Ω_0 for the third set of experiments is inspired by the complex structure of Baby-Yoda (apprentice Grogu from Disney's Mandalorian TV series), and we use this geometry as an illustration of the flexibility and efficiency of our FEM-BEM approach, and the ability to approximate non-smooth fields from complex heterogeneous media. The total field induced by the Baby-Yoda based piecewise continuous refractive index illustrates the complexity of the wave propagation model (2.1).

We simulated numerical experiments using the quadratic ($\mathbb{P}_2$) and cubic ($\mathbb{P}_3$) spline elements for FEM, and for several different values for the BEM parameter N. Thus the number of BEM degrees of freedom (DoF) for the Γ boundary unknown function is $2N$ and, throughout this section, we denote L as the FEM DoF in Ω_2 and M as the number of Dirichlet constrained nodes on Σ. Clearly $M << L$ (since $M \approx \sqrt{L}$), and because Γ is smooth boundary, the spectral accuracy of the Nyström BEM implies that $2N << M$. Our FEM-BEM framework involving only relatively small algebraic linear systems (3.13a), for the $(2N + M)$ boundary unknowns, were solved iteratively using GMRES with a very low tolerance of 10^{-9}, to ensure that the reported errors corresponds to the method itself and not from an approximation of the algebraic system solutions.

For a desired level of accuracy, choices of the discretization parameters crucially depend on the wavelength of the problem, which in turn depends on the variable coefficient k^2n^2 of the model (2.1) and the size of computational regions for the main unknowns (that determine the DoF in algebraic systems). For the heterogeneous and unbounded region model problem (2.1), our efficient FEM-BEM framework reduces the computational regions to just bounded regions $\overline{\Omega_2}$ and Σ. We recall that if $\Omega_{2,\mathrm{diam}}$ denotes the diameter of the domain Ω_2 and $n_{\max}$ is the maximum value of the refractive index n, for our FEM-BEM framework, the FEM interior problem wavelength is $(k \times n_{\max} \times \Omega_{2,\mathrm{diam}})/(2\pi)$; and the BEM exterior problem wavelength is $(k \times \Gamma_{\mathrm{diam}})/(2\pi)$, where Γ_{diam} is the length of the artificial boundary curve Γ.

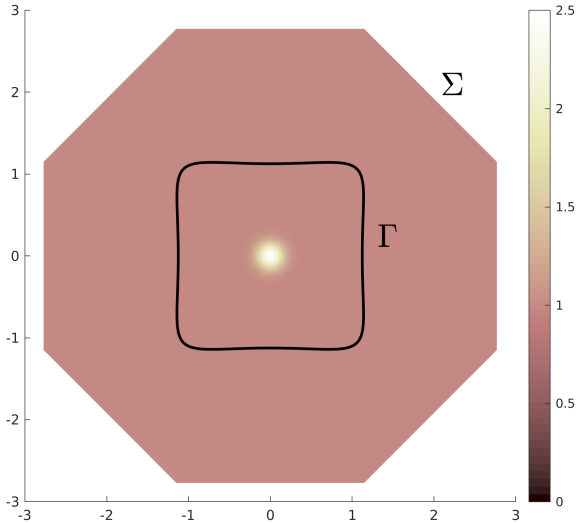

Figure 2: *Experiment #1 smooth radial refractive index function (with maximum at origin) and a decomposition framework comprising curves* Γ *and* Σ*. The octagonal shaped polygonal domain* Ω_2*, with boundary* Σ*, is centered at origin and has circumradius 3.* Γ *is a smooth rounded-squared curve. The framework illustrate flexibility of artificial curve choices* Γ *and* Σ*.*

5.1 Experiment #1 (Smooth refractive index and smooth solution)

In the first set of experiments we choose the example refractive index induced by a Gaussian smoothing window function in the radial variable $r = |\boldsymbol{x}|$, $\boldsymbol{x} = (x, y) \in \mathbb{R}^2$:

$$n^2(x, y) \equiv n^2(r) = \begin{cases} 1 + 1.5\exp(-40r^2), & r \in [0, 1], \\ 1, & r > 1. \end{cases}$$

Since the value above function at $r = 1$ is less than $1 + \epsilon$ (where ϵ is the machine-epsilon), the refractive index can be considered as numerically smooth. This example function and our numerical experiments FEM-BEM decomposition framework with artificial curves are demonstrated in Figure 2. For the first set of experiments to demonstrate accuracy of the FEM-BEM approximations, the incident wave is a plane wave with wavenumber $k = 5$ and direction $\widehat{\boldsymbol{d}} = (1, 0)$. The rounded-square smooth curve Γ in Figure 2 is obtained using the 2π-periodic parametrization

$$\mathbf{x}(t) = \frac{4}{5\sqrt{2}}((1+\cos^2 t)\cos t + (1+\sin^2 t)\sin t, -(1+\cos^2 t)\cos t + (1+\sin^2 t)\sin t), \quad t \in [0, 2\pi]. \tag{5.2}$$

The initial (coarsest) grid comprise 4,512 triangles for both $\mathbb{P}_2$ and $\mathbb{P}_3$ elements and we used up to five uniform refinements. For N, the discrete parameter for the BEM part, the initial value $N_0 = 20$ was refined five times (by doubling). Accuracy of the the first set of simulated FEM and BEM solutions in the H^1-norm are displayed in Table 1. According to Theorem 4.9, for the Experiment #1 choices, the estimated rate of convergence of the combined FEM-BEM solution in the H^1-error is dominated by the optimal rate h^d in the $\mathbb{P}_d$ element space for $d = 2, 3$. For fixed and sufficiently high $N(= 160)$ case, this estimated convergence can be observed from the last row in Table 1, as the FEM mesh size h is reduced by two with mesh refinement (and corresponding L increase) the FEM solution errors decrease approximately by $(1/2)^d$-times, for

$d = 2, 3$. The spectral accuracy of the BEM solution can be observed from the last column in Table 1 with high accuracy achieved using relative small BEM DoF. For the first set of experiments, the GMRES iterations convergence was attained using a small number (m) of iterations with $16 \leq m \leq 20$.

N \ L	9,185		36,417		145,025		578,817		2,312,705	
	FEM	BEM	FEM	BEM	FEM	BEM	FEM	BEM	FEM	BEM
020	2.4e-01	6.4e-02	6.1e-02	5.5e-02	1.5e-02	5.4e-02	3.7e-03	5.4e-02	2.2e-05	5.4e-02
040	2.4e-01	3.7e-02	6.1e-02	5.7e-03	1.5e-02	7.0e-04	3.7e-03	3.6e-04	2.1e-05	3.5e-04
080	2.4e-01	2.8e-02	6.1e-02	4.3e-03	1.5e-02	4.6e-04	3.7e-03	6.7e-05	2.1e-05	4.8e-06
160	2.4e-01	2.7e-02	6.1e-02	2.7e-03	1.5e-02	2.4e-04	3.7e-03	3.2e-05	2.1e-05	2.5e-06

N \ L	20,545		81,697		325,825		1,301,377		5,201,665	
	FEM	BEM	FEM	BEM	FEM	BEM	FEM	BEM	FEM	BEM
020	1.2e-02	5.6e-02	1.5e-03	5.6e-02	2.6e-04	5.6e-02	2.1e-04	5.6e-02	2.0e-04	5.06-02
040	1.2e-02	1.3e-03	1.4e-03	3.8e-04	1.7e-04	3.4e-04	2.1e-05	3.4e-04	1.1e-06	3.4e-04
080	1.2e-02	1.1e-03	1.4e-03	1.3e-04	1.7e-04	6.9e-06	2.1e-05	9.2e-08	1.1e-06	2.7e-08
160	1.3e-02	1.2e-03	1.4e-03	9.5e-05	1.7e-04	3.5e-06	2.1e-05	7.0e-08	1.1e-06	1.9e-08

Table 1: *Experiment #1 results ($k = 5$). Estimated H^1- error for total wave in Ω_2 (FEM-part) and for scattered wave away from Γ (BEM-part) for $\mathbb{P}_2$ (top), $\mathbb{P}_3$ (bottom) elements.*

For the case $k = 5$, the Experiment #1 interior problem wavelength is approximately 6.2. We also performed higher frequency simulations, with $k = 10, 20$, we observed similar FEM-BEM convergence rates similar to that in Table 1 for the smooth solution Experiment #1. For the non-smooth solution cases, as we shall demonstrate below for $k = 5, 10, 20$ cases, sufficiently fine FEM mesh and also high-order finite elements are required to obtained good accuracy.

5.2 Experiment #2 (Janus-type configuration non-smooth solution)

For this set of experiments, a disconnected heterogeneous medium illustrated in Figure 3, is induced by a collection of non-smooth (polygonal) Janus particles of different sizes, and each particle is designed using two distinct materials/liquids [34]. As described in Section 1, this is a model problem for the so-called Janus configuration which has received much attention in recent years. For the Figure 3 Janus configuration based second set of numerical experiments, we used the following non-smooth (piecewise-continuous) refractive index function, defined in the full unbounded wave propagation medium, for $(x, y) \in \mathbb{R}^2$, as

$$n(x,y) = \begin{cases} 1.333 & (x,y) \in \text{first halves of Janus particles,} \\ 1.496 & (x,y) \in \text{second halves of Janus particles,} \\ 1 & \text{Outside the collection of Janus particles.} \end{cases} \tag{5.3}$$

In (5.3), we recall that the numbers 1.333 and 1.496 correspond to, respectively, the refractive index of water and toluene at 20C; such two chemicals mix have been used in the literature to build Janus configurations [34]. Janus configuration based numerical investigations [21, 29, 33, 34, 38, 39] have been mainly restricted to simple shapes, and results in this section further demonstrate that such (shape, size, and number of particles) restrictions can be removed

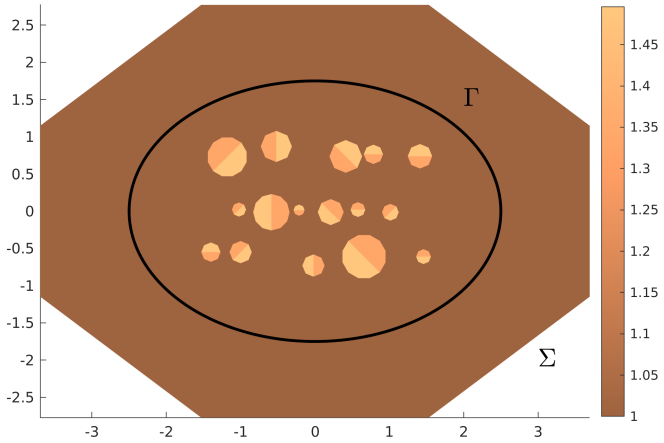

Figure 3: *Experiment #2 setup comprises a Janus-type configuration with* 16 *Janus particles (each having a local piecewise-constant refractive index) of distinct sizes and non-smooth shapes. The FEM octagonal shaped polygonal domain* Ω_2*, with artificial boundary* Σ*, is centered at origin and has circumradius 3.5. The BEM smooth artificial boundary* Γ *is an elliptical curve and the ellipse circumscribes the multi-particle heterogeneous Janus configuration.*

using efficient algorithms that can accommodate complex heterogeneous structures with efficient decomposition framework. The simulated Experiment #2 configuration with a decomposition framework is depicted in Figure 3.

For these experiments we chose medium and high frequencies with $k = 5, 10, 20$ (corresponding to, respectively, approximate interior problem wavelengths $8.3, 16.6, 33.2$) with the coarse mesh for FEM comprising 1401 triangles. For a fixed incident plane wave case, we took the direction to be $\widehat{\boldsymbol{d}} = (1, 0)$. For simulating the OA-DSCS of the Janus configuration, we chose one thousand equally-spaced incident directions $\widehat{\boldsymbol{d}}(\phi)$ surrounding the configuration that corresponds to one thousand of the configuration orientations, with equally spaced orientation angles $\phi \in [0, 2\pi)$, starting from the initial Janus configuration in Figure 3 (with $\phi = 0$).

The choice of equally spaced direction angles facilitates high-order approximations to the integral in (2.4) to compute the OA-DSCS using the rectangle quadrature. We recall Remark 2.2 to highlight that our discrete FEM-BEM algorithm is efficient for computing solutions with a large number of incident waves. The first set of experiments for the Janus configuration is performed with $\phi = 0$ to ensure that high-order approximations of the DSCS integrand in (2.4) can be computed using our FEM-BEM algorithm. We recall that computation of the far-field in (2.4) is a smooth post-processing of the field density on Γ, and hence we expect that the accuracy of far-field approximations should be better, after ensuring convergence and good accuracy of the Janus configuration based FEM-BEM solution.

Our simulation results (for $k = 5, 10, 20$), demonstrating the FEM-BEM solution accuracy for the ($\phi = 0$) Janus configuration in Figure 3, obtained using the $\mathbb{P}_2$ elements are in Table 2, and the counterpart $\mathbb{P}_3$ elements results are in Table 3. Because of the restricted regularity of the exact scattered field induced by only piecewise-continuity of the refractive index in (5.3), it can be observed from Tables 2-3, the limited (second-order) rate of convergence of the FEM solution does not improve by using $\mathbb{P}_3$ elements compared to that for $\mathbb{P}_2$ elements. However, because of the restricted regularity, it is important to use high-order $\mathbb{P}_3$ elements especially

N \ L	5,531		21,981		87,641		350,001		1,398,881	
	FEM	BEM	FEM	BEM	FEM	BEM	FEM	BEM	FEM	BEM
020	1.6e+00	2.0e+00	3.2e-01	2.7e-01	7.8e-02	2.3e-01	1.9e-02	2.3e-01	5.2e-03	2.3e-01
040	1.6e+00	1.9e+00	3.2e-01	1.3e-01	7.8e-02	1.3e-02	1.9e-02	1.2e-03	4.7e-03	6.1e-04
080	1.6e+00	1.8e+00	3.1e-01	1.2e-01	7.7e-02	9.6e-03	1.9e-02	8.7e-04	4.7e-03	8.4e-05
160	1.6e+00	1.8e+00	3.1e-01	1.1e-01	7.7e-02	7.6e-03	1.9e-02	7.9e-04	4.7e-03	5.4e-05

N \ L	5,531		21,981		87,641		350,001		1,398,881	
	FEM	BEM	FEM	BEM	FEM	BEM	FEM	BEM	FEM	BEM
020	7.9e+01	7.8e+01	4.9e+01	4.4e+01	4.3e+01	4.0e+01	4.0e+01	4.0e+01	1.6e+01	4.0e+01
040	7.2e+01	5.5e+01	1.7e+01	1.7e+01	5.3e+00	5.7e+00	5.6e-01	5.6e-01	5.4e-01	3.8e-02
080	7.3e+01	5.5e+01	1.6e+01	1.7e+01	5.1e+00	5.4e+00	4.8e-01	4.8e-01	4.8e-01	3.2e-02
160	7.3e+01	5.6e+01	1.6e+01	1.7e+01	4.8e+00	5.1e+00	4.5e-01	4.5e-01	4.5e-01	2.8e-02

N \ L	5,531		21,981		87,641		350,001		1,398,881	
	FEM	BEM	FEM	BEM	FEM	BEM	FEM	BEM	FEM	BEM
020	6.0e+02	2.3e+02	1.5e+03	5.75e+02	1.1e+03	4.6e+02	1.6e+03	6.3e+02	1.4e+03	5.4e+02
040	4.5e+02	1.5e+02	2.8e+02	1.35e+02	3.6e+02	1.7e+02	1.3e+03	7.2e+02	1.6e+03	8.5e+02
080	3.3e+02	1.2e+02	2.3e+02	1.14e+02	4.1e+01	2.2e+01	1.2e+01	4.7e+00	1.2e+00	4.6e-01
160	3.2e+02	1.2e+02	2.4e+02	1.17e+02	4.0e+01	2.2e+01	1.2e+01	4.5e+00	1.1e+00	4.2e-01

Table 2: *Experiment #2 results using $\mathbb{P}_2$ elements with $k = 5$ (top), $k = 10$ (mid), and $k = 20$ (bottom). Estimated H^1- error for the total wave in Ω_2 (FEM-part) and for the scattered wave away from Γ (BEM-part).*

for the higher frequency ($k > 10$) cases. This is because, for example with $k = 20$ (despite using over one million FEM DoF L), the $\mathbb{P}_2$ elements based FEM solutions with over 100% errors observed in the last row of Table 2 are not acceptable, and for the same situation the $\mathbb{P}_3$ elements provide much better accurate solutions.

In Figure 4 we visualize the total field in Ω_2 and the scattered field in the overlapped region $(\mathbb{R}^2 \setminus \overline{\Omega}_1) \cap \Omega_2$, and in Figure 5, we demonstrate the constraint of (numerically) matching the FEM and BEM solutions in the overlapped region by plotting the error in the region in log-scale. These sets of experiments illustrate the computational difficulties associated with Janus configurations based wave models, especially taking into account that linear $\mathbb{P}_1$ elements are standard for pure FEM algorithms (that do not satisfy the SRC) [24].

Further advantages of our FEM-BEM algorithm to compute high-order approximations to smooth far-fields, and hence the DSCS (with fixed incident direction angle $\phi = 0$), are demonstrated in Table 4. Recall that the far-field is a smooth function defined on $\mathbb{S}^1$, and the uniform norm errors in the far-field were approximated by evaluating the DSCS at 1440 equally distributed points in $\mathbb{S}^1$. Because of the smooth post-processing of the FEM-BEM solutions to compute far-fields, similar to the $k = 5$ results in Table 4, we observed higher accuracy for the $k = 10, 20$ cases compared to the FEM-BEM solutions accuracy. We conclude the Experiment #2 results in Figure 6 showing the OA-DSCS as a function of the observed scattering DSCS angles (in degrees) for $k = 5, 10, 20$.

N \ L	12,391		49,351		196,981		787,081		3,146,641	
	FE	BEM	FE	BEM	FE	BEM	FE	BEM	FE	BEM
020	1.4e-01	3.3e-01	1.7e-02	3.1e-01	3.1e-03	3.1e-01	2.1e-03	3.1e-01	2.9e-03	3.1e-01
040	1.3e-01	9.4e-02	1.7e-02	5.2e-03	2.3e-03	8.2e-04	3.9e-04	8.0e-04	7.9e-05	8.0e-04
080	1.3e-01	7.8e-02	1.7e-02	4.2e-03	2.3e-03	2.1e-04	3.9e-04	1.1e-05	7.9e-05	1.5e-06
160	1.3e-01	7.8e-02	1.7e-02	3.7e-03	2.3e-03	2.0e-04	3.9e-04	1.2e-05	7.9e-05	1.5e-06

N \ L	12,391		49,351		196,981		787,081		3,146,641	
	FE	BEM	FE	BEM	FE	BEM	FE	BEM	FE	BEM
020	4.9e+01	5.7e+01	4.3e+01	5.2e+01	4.3e+01	5.2e+01	4.3e+01	5.2e+01	4.3e+01	5.2e+01
040	8.3e+00	1.2e+01	9.8e-01	1.3e+00	5.2e-02	5.8e-02	7.5e-03	9.6e-03	5.2e-03	8.9e-03
080	7.9e+00	1.1e+01	1.0e+00	1.4e+00	4.1e-02	3.7e-02	4.3e-03	1.3e-03	5.8e-04	7.8e-05
160	8.0e+00	1.1e+01	9.6e-01	1.3e+00	4.0e-02	3.5e-02	4.2e-03	6.5e-04	5.8e-04	5.0e-05

N \ L	12,391		49,351		196,981		787,081		3,146,641	
	FE	BEM	FE	BEM	FE	BEM	FE	BEM	FE	BEM
020	1.5e+03	6.7e+02	2.5e+03	1.2e+03	1.4e+03	6.7e+02	1.4e+03	6.5e+02	1.4e+03	6.5e+02
040	9.6e+02	5.3e+02	7.5e+02	4.1e+02	1.5e+03	1.0e+03	1.6e+03	1.1e+03	1.6e+03	1.1e+03
080	6.3e+02	3.8e+02	6.3e+01	4.1e+01	1.4e+00	6.9e-01	7.9e-02	2.5e-02	1.4e-02	6.5e-03
160	6.6e+02	3.9e+02	6.0e+02	3.9e+01	1.4e+00	7.3e-01	7.7e-02	2.4e-02	8.2e-03	9.9e-04

Table 3: *Experiment #2 results using $\mathbb{P}_3$ elements with $k = 5$ (top), $k = 10$ (mid), and $k = 20$ (bottom). Estimated H^1- error for the total wave in Ω_2 (FEM-part) and for the scattered wave away from Γ (BEM-part).*

N \ L	5,531	21,981	87,641	350,001	1,398,881
010	5.15e+00	4.91e+00	4.89e+00	4.89e+00	4.89e+00
020	4.37e-01	2.77e-02	3.14e-03	1.65e-03	1.33e-03
040	4.12e-01	2.53e-02	1.04e-03	2.93e-04	3.34e-05
080	4.08e-01	2.60e-02	1.58e-03	1.26e-04	2.76e-05
160	4.04e-01	2.58e-02	1.67e-03	1.39e-04	2.83e-05

N/L	12,391	49,351	196,981	787,081	3,146,641
010	4.89e+00	4.89e+00	4.89e+00	4.89e+00	4.89e+00
020	5.01e-03	1.17e-03	1.31e-03	1.36e-03	1.36e-03
040	1.03e-02	4.89e-04	2.15e-05	3.87e-07	7.79e-08
080	1.23e-02	4.47e-04	3.18e-05	7.21e-07	8.25e-08
160	1.30e-02	3.45e-04	3.88e-05	1.07e-06	4.94e-08

Table 4: *Experiment #2 estimated DSCS uniform norm errors, for $k = 5$, with $\mathbb{P}_2$ (top) and $\mathbb{P}_3$ (bottom) elements and $\phi = 0$ (i.e., with $\boldsymbol{d} = (1, 0)$ in the incident plane wave).*

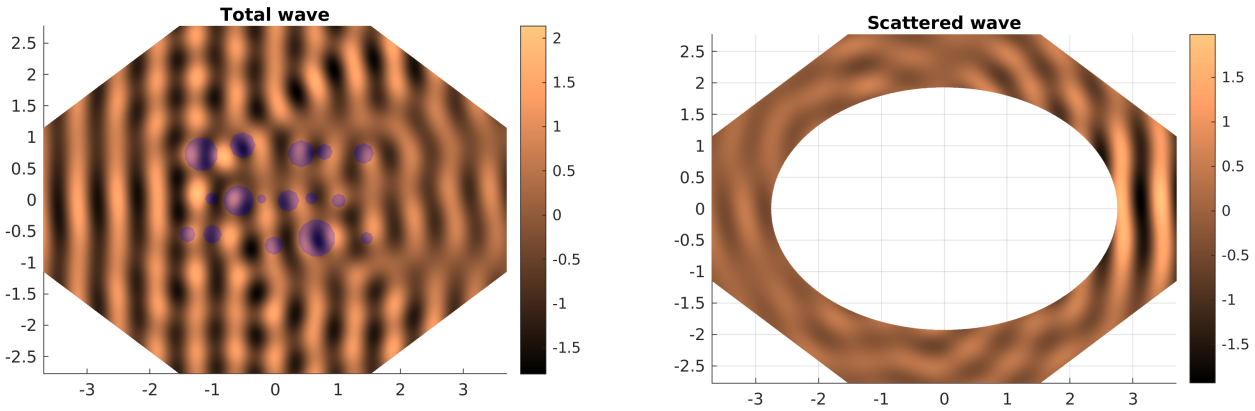

Figure 4: *Experiment #2 ($k = 20$). Computed total wave (left) and scattered wave (right) using $\mathbb{P}_3$-finite elements with $698,880$ elements and $1,398,881$ nodes, and using a spectral BEM with $N = 80$.*

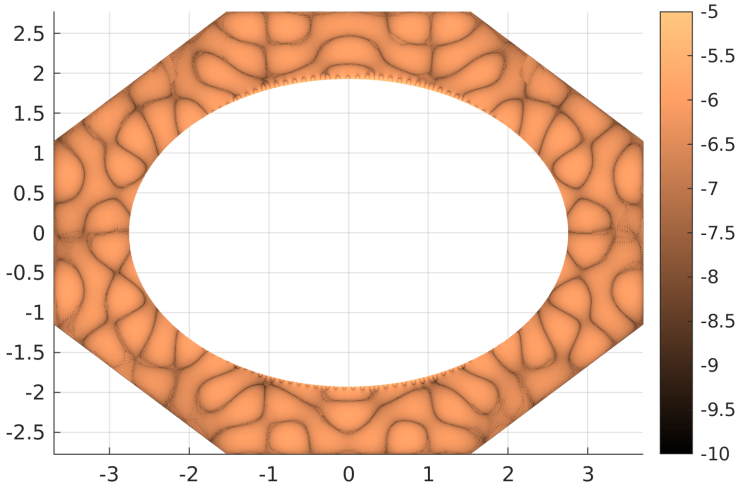

Figure 5: *Experiment #2 (with parameter values as in Figure 4. Absolute difference in log-scale between BEM-computed and FEM-computed approximation solutions in the overlapped region $(\mathbb{R}^2 \setminus \overline{\Omega}_1) \cap \Omega_2$.*

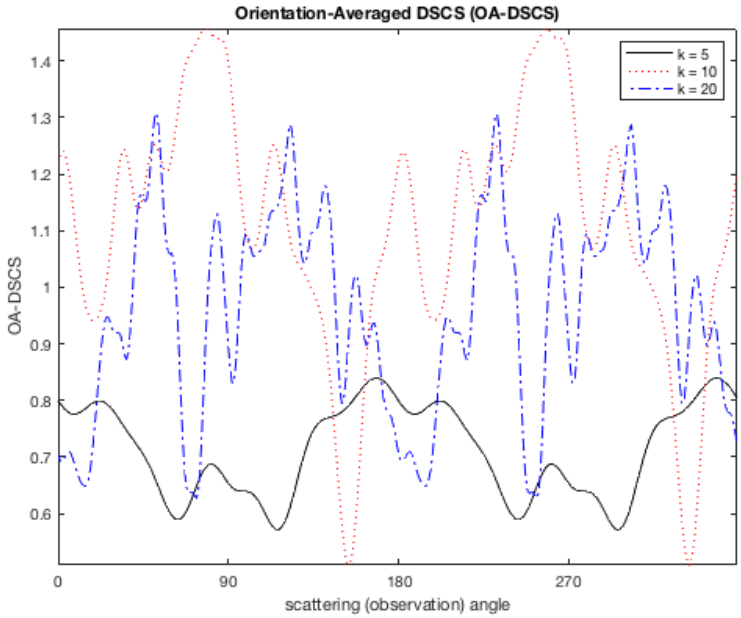

Figure 6: Orientation-Averaged DSCS for Experiment #2

5.3 Experiment #3 (A Baby-Yoda shaped heterogeneous region)

In this set of experiments, we demonstrate flexibility of our FEM-BEM algorithm with complex structured heterogeneous regions. To this end, we consider a Baby-Yoda like domain, depicted in Figure 7 on which the refraction index function is defined. The function is taken to be piecewise-constant at distinct parts of the domain with values indicated in Figure 7, leading to the total field solution u with limited regularity. In Figure 7 we also show the curve Γ taken for our BEM computations, which is similar to the smooth curve in Experiment #1 with some rescaling; and the choice of Σ is such that the FEM computational domain Ω_2 is a rectangle. Similar to the first two sets of experiments, we simulate the model with wavenumbers $k = 5, 10, 20$, and for the configuration in Figure 7 these values respectively correspond to $9.2, 18.4, 36.8$ interior wavelengths region Ω_2.

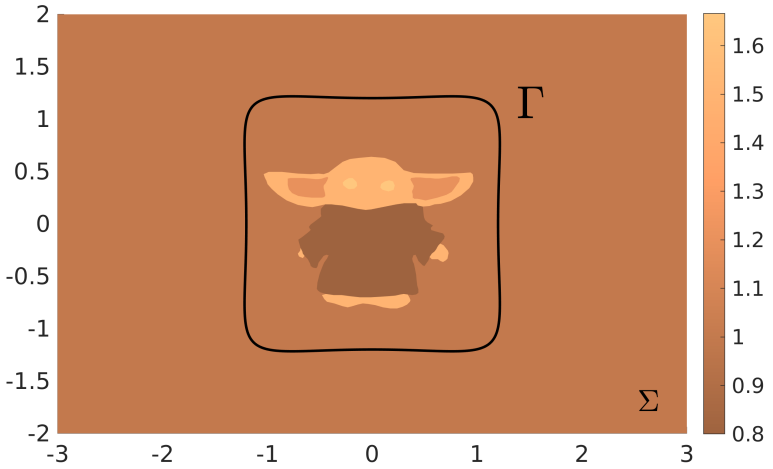

Figure 7: *Experiment #3 setup with Baby-Yoda heterogeneous region.*

Similar to the first two sets of experiments, sample results in Table 5 demonstrate the power of our overlapped FEM-BEM algorithm even for the case of simulation of non-smooth wave fields induced by only piecewise-continuous refractive index in complicated heterogeneous regions. Another marked advantage of our FEM-BEM algorithm is the low number of iterations required for convergence of the GMRES to iteratively solve the resulting interface algebraic linear systems (3.13a). In particular, as can be observed in Table 6, for each fixed wavenumber k the number of required GMRES iterations is independent of the numbers of FEM-BEM DoFs (level of discretizations). In addition, even as the frequency is doubled the required iterations grow only mildly (to achieve a fixed error tolerance), and because of the well-conditioning the interface system (3.13a), even for the high-frequency case, less than 100 GMRES iterations are required without using any preconditioner. We conclude the numerical experiments section with visualizations in Figure 8 for (i) the total field in Ω_2; (ii) the scattered field in the overlapped region $\Omega_{12} = (\mathbb{R}^2 \setminus \overline{\Omega}_1) \cap \Omega_2$; and (iii) accurate matching of the FEM and BEM solutions in the overlapped region in Figure 9.

N \ L	114,094		455,785		1,821,961	
	FE	BEM	FE	BEM	FE	BEM
020	3.1e-02	3.0e-01	2.0e-02	3.0e-01	1.6e-02	3.0e-01
040	2.7e-02	2.2e-03	1.4e-02	2.0e-03	6.2e-03	2.0e-03
080	2.7e-02	9.6e-04	1.4e-02	2.4e-04	6.2e-03	5.2e-05
160	2.7e-02	9.5e-04	1.4e-02	2.4e-04	6.2e-03	5.2e-05

N \ L	114,094		455,785		1,821,961	
	FE	BEM	FE	BEM	FE	BEM
020	2.1e+01	1.9e+01	2.1e+01	1.9e+01	2.1e+01	1.9e+01
040	8.5e-02	2.8e-02	2.9e-02	5.7e-02	1.3e-02	5.1e-03
080	8.5e-02	2.7e-02	2.9e-02	2.1e-03	1.3e-02	2.1e-04
160	8.5e-02	2.6e-02	2.9e-02	2.0e-03	1.3e-02	2.1e-04

N \ L	114,094		455,785		1,821,961	
	FE	BEM	FE	BEM	FE	BEM
020	1.7e+02	1.1e+02	1.7e+02	1.1e+02	1.7e+02	1.1e+02
040	5.1e+00	4.3e+00	5.0e+01	4.4e+00	5.0e+01	4.4e+00
080	1.0e+00	2.7e-01	1.3e-01	6.5e-03	3.0e-02	8.8e-04
160	1.0e+00	2.7e-01	1.3e-01	6.2e-03	3.0e-02	8.6e-04

Table 5: *Experiment #3 results using $\mathbb{P}_3$ elements with $k = 5$ (top), $k = 10$ (mid), and $k = 20$ (bottom). Estimated H^1- error for the total wave in Ω_2 (FEM-part) and for the scattered wave away from Γ (BEM-part).*

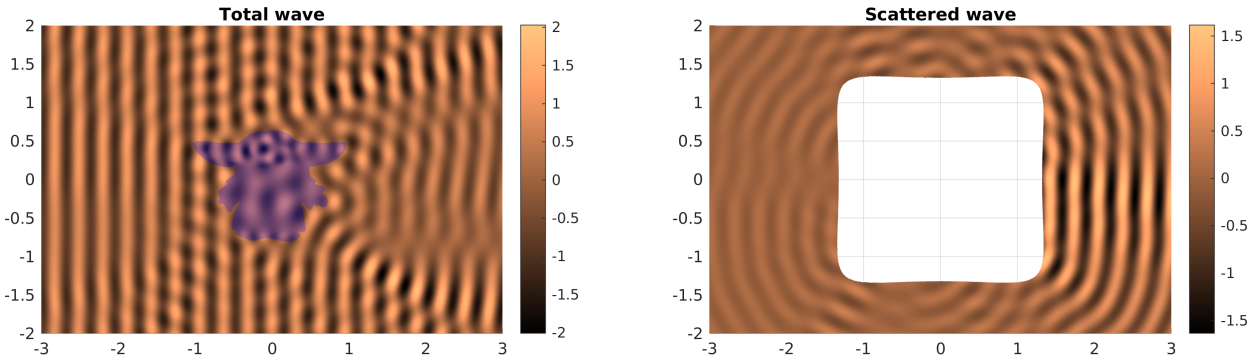

Figure 8: *Experiment #3 ($k = 20$). Computed total wave (left) and scattered wave (right) using $\mathbb{P}_3$-finite elements with $478,464$ elements and $1,821,961$ nodes, and using a spectral BEM with $N = 80$.*

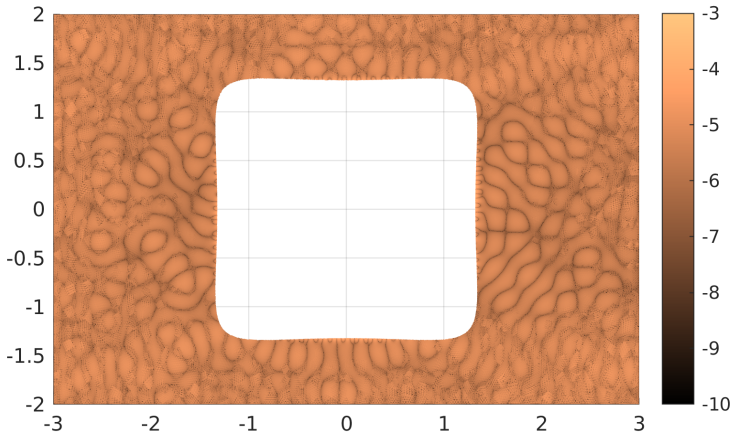

Figure 9: *Experiment #3 (with parameter values as in Figure 8. Absolute difference in log-scale between BEM-computed and FEM-computed approximation solutions in the overlapped region $\Omega_{12} = (\mathbb{R}^2 \setminus \overline{\Omega}_1) \cap \Omega_2$.*

N \ L	48,137			192,153			767,825			3,069,729		
	k=5	k=10	k=20	k=5	k=10	k=20	k=5	k=10	k=20	k=5	k=10	k=20
020	22	38	40	22	38	40	22	38	040	22	38	40
040	22	38	67	22	38	67	22	38	067	22	38	67
080	22	38	67	22	38	67	22	38	067	22	38	67
160	22	38	67	22	38	67	22	38	067	22	38	67

N \ L	114,094			455,785			1,821,961		
	k=5	k=10	k=20	k=5	k=10	k=20	k=5	k=10	k=20
020	22	38	40	22	38	40	22	38	40
040	22	38	67	22	38	67	22	38	67
080	22	38	67	22	38	67	22	38	67
160	22	38	67	22	38	67	22	38	67

Table 6: *Experiment #3. Total number of GMRES iterations for convergence (with tolerance* 10^{-8}*) using* $\mathbb{P}_2$ *(top) and* $\mathbb{P}_3$ *(bottom) elements. For each fixed* k*, the total number of required GMRES iterations is independent of* N *and* L *and grows mildly with respect to increase in the wavenumber* k*.*

Acknowledgement

We sincerely thank the anonymous referees for suggestions which helped to improve the paper. The first author (Domínguez) is supported by the project MTM2017-83490-P. The second author (Ganesh) gratefully acknowledges the support of the Simons Foundation.

References

[1] R.A. Adams and J.J.F. Fournier. *Sobolev spaces*, volume 140 of *Pure and Applied Mathematics (Amsterdam)*. Elsevier/Academic Press, Amsterdam, second edition, 2003.

[2] S. Bertoluzza. The discrete commutator property of approximation spaces. *C. R. Acad. Sci. Paris Sér. I Math.*, 329(12):1097–1102, 1999.

[3] H. Brakhage and P. Werner. Über das Dirichletsche Aussenraumproblem für die Helmholtzsche Schwingungsgleichung. *Arch. Math.*, 16:325–329, 1965.

[4] S.C. Brenner and L.R. Scott. *The mathematical theory of finite element methods*, volume 15 of *Texts in Applied Mathematics*. Springer, New York, third edition, 2008.

[5] P.G. Ciarlet. *The Finite Element Method for Elliptic Problems*. Classics in Applied Mathematics. Society for Industrial and Applied Mathematics, 2002.

[6] D. Colton and R. Kress. *Inverse Acoustic and Electromagnetic Scattering Theory*. Springer, 4th edition, 2019.

[7] M. Costabel. Boundary integral operators on Lipschitz domains: elementary results. *SIAM J. Math. Anal.*, 19(3):613–626, 1988.

[8] J. Coyle and P. Monk. Scattering of time-harmonic electromagnetic waves by anisotropic in homogeneous scatterers or impenetrable obstacles. *SIAM J. Math. Anal.*, 37:1590–1617, 2004.

[9] P. G. de Gennes. Soft Matter (Nobel Lecture). *Angew. Chem. Int. Ed. Engl.*, 31:842–845, 1992.

[10] V. Domínguez, M. Ganesh, and F.J. Sayas. An overlapping decomposition framework for wave propagation in heterogeneous and unbounded media: Formulation, analysis, algorithm, and simulation. *J. Comput. Phys.*, 403:109052, 2020.

[11] V. Domínguez and F.-J. Sayas. Stability of discrete liftings. *C. R. Math. Acad. Sci. Paris*, 337(12):805–808, 2003.

[12] V. Domínguez and C. Turc. High order Nyström methods for transmission problems for Helmholtz equations. In *Trends in differential equations and applications*, volume 8 of *SEMA SIMAI Springer Ser.*, pages 261–285. Springer, [Cham], 2016.

[13] M. Ganesh and S. C. Hawkins. Algorithm 975: TMATROM—a T-matrix reduced order model software. *ACM Trans. Math. Softw.*, 44:9:1–9:18, 2017.

[14] M. Ganesh, S. C. Hawkins, and R. Hiptmair. Convergence analysis with parameter estimates for a reduced basis acoustic scattering T-matrix method. *IMA J. Numer. Anal.*, 32:1348–1374, 2012.

[15] M. Ganesh and C. Morgenstern. High-order FEM-BEM computer models for wave propagation in unbounded and heterogeneous media: application to time-harmonic acoustic horn problem. *J. Comput. Appl. Math.*, 307:183–203, 2016.

[16] M. Ganesh and C. Morgenstern. High-order FEM domain decomposition models for high-frequency wave propagation in heterogeneous media. *Comp. Math. Appl. (CAMWA)*, 75:1961–1972, 2018.

[17] M. Ganesh and C. Morgenstern. A coercive heterogeneous media Helmholtz model: formulation, wavenumber-explicit analysis, and preconditioned high-order FEM. *Numerical Algorithms*, 83:1441–1487, 2020.

[18] C. Geuzaine and J.-F. Remacle. Gmsh: A 3-D finite element mesh generator with built-in pre- and post-processing facilities. *International Journal for Numerical Methods in Engineering*, 79:1309 – 1331, 2009.

[19] A. Gillman, A. H. Barnett, and P.-G. Martinsson. A spectrally accurate direct solution technique for frequency-domain scattering problems with variable media. *BIT Numerical Mathematics*, 55(1):141–170, 2015.

[20] P. Grisvard. *Elliptic problems in nonsmooth domains*, volume 69 of *Classics in Applied Mathematics*. Society for Industrial and Applied Mathematics (SIAM), Philadelphia, PA, 2011.

[21] S. C. Hawkins, T. Rother, and J. Wauer. Numerical study of acoustic scattering by Janus spheres. *J. Acoust. Soc. Am.*, 147:4097, 2020.

[22] C. Hazard and M. Lenoir. On the solutions of time-harmonic scattering problems for maxwell's equations. *SIAM J. Math. Anal.*, 27:1597–1630, 1996.

[23] G. C. Hsiao and W. L. Wendland. *Boundary integral equations*, volume 164 of *Applied Mathematical Sciences*. Springer-Verlag, Berlin, 2008.

[24] F. Ihlenburg. *Finite element analysis of acoustic scattering*, volume 132 of *Applied Mathematical Sciences*. Springer-Verlag, New York, 1998.

[25] A. Jami and M. Lenoir. A variational formulation for exterior problems in linear hydrodynamics. *Comput. Methods Appl. Mech. Engrg.*, 16:341–359, 1978.

[26] A. Kirsch and P. Monk. Convergence analysis of a coupled finite element and spectral method in acoustic scattering. *IMA J. Numer. Anal.*, 10(3):425–447, 1990.

[27] A. Kirsch and P. Monk. An analysis of the coupling of finite-element and Nyström methods in acoustic scattering. *IMA J. Numer. Anal.*, 14(4):523–544, 1994.

[28] R. Kress. *Linear integral equations*, volume 82 of *Applied Mathematical Sciences*. Springer, New York, third edition, 2014.

[29] M. Lattuada and A. Hatton. Synthesis, properties and applications of janus nanoparticles. *Nano Today*, 6:286–308, 2011.

[30] W. McLean. *Strongly elliptic systems and boundary integral equations*. Cambridge University Press, Cambridge, 2000.

[31] J.-C. Nédélec. *Acoustic and electromagnetic equations*, volume 144 of *Applied Mathematical Sciences*. Springer-Verlag, New York, 2001. Integral representations for harmonic problems.

[32] J. A. Nitsche and A. H. Schatz. Interior estimates for Ritz-Galerkin methods. *Math. Comp.*, 28:937–958, 1974.

[33] T. Rother. *Sound Scattering on Spherical Objects*. Springer, New York, 2020.

[34] T. M. Ruhland, A. H. Gröschel, N. Ballard, T. S. Skelhon, A.Walther, A. H. E. Müller, and S. A. F. Bon. Influence of Janus particle shape on their interfacial behavior at liquid-liquid interfaces. *Langmuir*, 29:1388–1394, 2013.

[35] J. Saranen and G. Vainikko. *Periodic integral and pseudodifferential equations with numerical approximation*. Springer Monographs in Mathematics. Springer-Verlag, Berlin, 2002.

[36] F. J. Sayas. The validity of Johnson-Nédélec's BEM-FEM coupling on polygonal interfaces. *SIAM Review*, 55:131–146, 2013.

[37] L.R. Scott and S. Zhang. Finite element interpolation of nonsmooth functions satisfying boundary conditions. *Math. Comp.*, 54(190):483–493, 1990.

[38] M. Vafaeezadeh and W. R. Thiel. Janus interphase catalysts for interfacial organic reactions. *J. Mol. Liq.*, 315:113735, 2020.

[39] J. Zhang, A. Gryzbowski, and Granick. Janus particle synthesis, assembly and application. *Langmuir*, 33:6964–6977, 2017.

A Sobolev convergence estimates for some projections

In this section we collect some useful results for projections on finite element spaces. The first set of results is concerned with finite element spaces on polygonal compact closed boundaries in $\mathbb{R}^2$. There finite element spaces are inherited by taking Dirichlet trace of finite element spaces on triangular meshes. We finish this section proving a commutation property for Scott-Zhang type projections, which is required in Appendix B for deriving superconvergence results of the finite element solution in stronger norms that are also valid in three dimensions. We think that most of the described results here belong to the folklore in finite element analysis. We include results below for the sake of completeness.

A.1 Projections on polygonal boundary finite element spaces

Let Σ be a polygonal simply connected closed curve with interior $\Omega \subset \mathbb{R}^2$. We consider $\{\mathcal{T}_h\}_{h\geq 0}$ a sequence of regular triangular meshes of Ω and denote by $\{\tau_h\}_{h\geq 0}$ that inherited on Σ. Without loss of generality we can assume that $h_\Sigma \approx h$, where h_Σ and h are the maximum, respectively, of the diameters of the elements of the grids $\mathcal{T}_h$ and τ_h. In addition, let

$$\mathbb{P}_{h,d} := \{u_h \in \mathcal{C}^0(\Omega) : \ u_h|_{T_h} \in \mathbb{P}_d\}, \qquad \gamma_\Sigma \mathbb{P}_{h,d}$$

denote the space of continuous finite elements space in Ω and its boundary Σ. We denote by

$$\mathrm{Q}_h : \mathcal{C}(\Omega) \to \mathbb{P}_{h,d}, \qquad \mathrm{Q}_\Sigma^h : \mathcal{C}(\Sigma) \to \gamma_\Sigma \mathbb{P}_{h,d}$$

the corresponding nodal (Lagrange) interpolation operators. Note that

$$\gamma_\Sigma \mathrm{Q}_h u_h = \mathrm{Q}_\Sigma^h \gamma_\Sigma u_h, \quad \forall u_h \in \mathbb{P}_{h,d}.$$

Our objectives in this section are twofold: (a) derive convergence estimates in the Sobolev norms $\|\cdot\|_{H^s(\Sigma)}$ for Q_Σ^h and $s \geq 0$ (see (2.5) for the definition we have taken for these spaces for $s > 1$); (b) define an alternative stable and convergent projection in weaker norms. In particular, we are interested in working with functions $H^{1/2}(\Sigma)$, the trace space, for which the interpolant cannot be defined since the space contains discontinuous functions. Next, we start with the first objective:

Proposition A.1. *For any $s \in [0,1]$ and $s \leq t < d+1$ with $t > 1/2$ there exists $C > 0$ such that*

$$\|\mathrm{Q}_\Sigma^h f_\Sigma - f_\Sigma\|_{H^s(\Sigma)} \leq C h_\Sigma^{t-s} \|f\|_{H^t(\Sigma)}. \tag{A.1}$$

Furthermore, for any $t > d+1$

$$\|\mathrm{Q}_\Sigma^h f_\Sigma - f_\Sigma\|_{H^s(\Sigma)} \leq C h_\Sigma^{d+1-s} \|f\|_{H^t(\Sigma)} \tag{A.2}$$

with $C > 0$ depending only on $s \in [0,1]$ and t.

Proof. We start with a classical result: for $s \in \{0,1\}$ and $t > \max\{1/2, s\}$ [5, Th. 3.1.6]

$$\|\mathrm{Q}_\Sigma^h f_\Sigma - f_\Sigma\|_{H^s(\Sigma)} \leq C' h_\Sigma^{t-s} \|f_\Sigma\|_{\mathcal{H}^t(\Sigma)}$$

where $\{\Sigma_\ell\}_\ell$ are the edges of Σ and $H^t(\Sigma_\ell)$ the corresponding classical Sobolev space, and

$$\|f_\Sigma\|^2_{\mathcal{H}^t(\Sigma)} := \sum_\ell \|f_\Sigma\|^2_{H^t(\Sigma_\ell)}.$$

For $t > 0$, with $t \neq 1, 2, \ldots$, we then use that the trace operator is also continuous in this norm

$$\|\gamma_\Sigma u\|_{\mathcal{H}^t(\Sigma)} \leq C\|u\|_{H^{t+1/2}(\Omega)}, \quad \forall u \in H^{t+1/2}(\Omega) \tag{A.3}$$

cf. [20, Th. 1.5.2.8] (the bound in (A.3) breaks precisely for $t = 0, 1, 2 \ldots$; see also [23, Th. 4.2.7]) which proves (A.1) for the considered non-integer values of t. By interpolation of Sobolev spaces, we can extend the result for any $t < d + 1$ and $s \in [0, 1]$, and hence (A.1) holds.

The bound (A.2) can be proven by starting from

$$\|\mathrm{Q}^h_\Sigma f_\Sigma - f_\Sigma\|_{H^s(\Sigma)} \leq C h_\Sigma^{d+1-s} \|f_\Sigma\|_{\mathcal{H}^{d+1+\varepsilon}(\Sigma)},$$

with $\varepsilon \in (0, 1)$ and again using (A.3). □

We will focus next on constructing a projection $\mathrm{P}^h_\Sigma : H^{1/2}(\Sigma) \to \gamma_\Sigma \mathbb{P}_{h,d}$ with same convergence rates in an extended Sobolev scale. A key fact in this construction is the existence of a Scott-Zhang-type projection cf. [37] (see also [11]). Specifically, there exists a continuous linear mapping $\Pi_{h,d} : H^s(\Omega) \to \mathbb{P}_{h,d}$, with $s > 1/2$, satisfying

1. Π_h is a projection:
$$\Pi_h v_h = v_h, \quad \forall v_h \in \mathbb{P}_{h,d}. \tag{A.4a}$$

2. The image of any element with null trace has null trace as well:
$$\gamma_\Sigma \Pi_h v = 0, \quad \text{if} \quad \gamma_\Sigma v = 0. \tag{A.4b}$$

3. It is quasi-local: for any triangle $K \in \mathcal{T}_h$,
$$\Pi_h v|_T = 0, \quad \text{if} \quad v|_{S_T} = 0, \text{ with } S_T := \bigcup_{\substack{T' \in \mathcal{T}_h \\ \overline{T}' \cap \overline{T} \neq \emptyset}} \overline{T}'. \tag{A.4c}$$

   Furthermore, for any $0 \leq s \leq t$ with $s \in [0, 3/2)$ and $1/2 < t \leq d + 1$ there exists $C = C(s, t)$ so that
$$\|\Pi_h v - v\|_{H^s(T)} \leq C h_T^{t-s} \|v\|_{H^t(S_T)}. \tag{A.4d}$$

   The constant $C(s, t)$ depends only on the chunkiness parameter of the grid. As consequence of (A.4d) we have
$$\left[\sum_{T \in \mathcal{T}_h} h_T^{2(s-t)} \|\Pi_h v - v\|^2_{H^s(T)}\right]^{1/2} \leq C\|v\|_{H^t(\Omega)}. \tag{A.4e}$$

Since for $s \in [0, 1/2) \cup [1, 3/2)$, we have

$$\|v\|_{H^s(\Omega)} \leq C \left[\sum_{T \in \mathcal{T}_h} \|v\|^2_{H^s(T)}\right]^{1/2}, \tag{A.5}$$

the simpler estimate

$$\|\Pi_h v - v\|_{H^s(\Omega)} \leq C h^{t-s} \|v\|_{H^t(\Omega)}. \tag{A.6}$$

can be derived from (A.4d), first for $s \in [0, 1/2) \cup [1, 3/2)$, and then can be extended for $s \in [1/2, 1)$ by interpolation of Sobolev spaces.

Remark A.2. The proof of (A.5) is based on working with the Slobodeckij form of the Sobolev norm: for non-integer $s > 0$ and for any Lipschitz domain $D \subset \mathbb{R}^m$

$$\|u\|^2_{H^s(D)} = \|u\|^2_{H^{\underline{s}}(D)} + \sum_{|\boldsymbol{\alpha}|=\underline{s}} \int_D \int_D \frac{|\partial_{\boldsymbol{\alpha}} u(\boldsymbol{x}) - \partial_{\boldsymbol{\alpha}} u(\boldsymbol{y})|}{|\boldsymbol{x}-\boldsymbol{y}|^{m+2(s-\underline{s})}} \mathrm{d}\boldsymbol{x}\,\mathrm{d}\boldsymbol{y},$$

where $\underline{s}$ is the largest integer less than s. Then, for $t \in (0, 1/2)$, it is easy to derive the estimate

$$\|v\|^2_{H^t(\Omega)} \leq C_{t,\Omega} \left[\sum_{T\in\mathcal{T}_h} \|v\|^2_{H^t(T)} + \int_T \frac{|v(\boldsymbol{x})|^2}{\rho(\boldsymbol{x},\partial T)^{2t}}\,\mathrm{d}\boldsymbol{x} \right]$$

where

$$\rho(\boldsymbol{x},\partial T) = \inf_{\boldsymbol{y}\in\partial T} |\boldsymbol{x}-\boldsymbol{y}|.$$

A Hardy-type inequality (see [30, Lemma 3.32]) allows to bound the above integral term by

$$\int_T \frac{|v(\boldsymbol{x})|^2}{\rho(\boldsymbol{x},\partial T)^{2t}}\,\mathrm{d}\boldsymbol{x} \leq C\|v\|^2_{H^t(T)}.$$

The constant C appearing above depends on t and on the chunkiness parameter of T. This inequality does not hold for $t \in [1/2, 1)$ since the last integral in the left hand side is expected to be non-convergent. The result for $t > 1$ is a simple extension of this argument.

The last ingredient is a right inverse of the trace operator $\mathrm{R}_{\Sigma\Omega} : H^s(\Sigma) \to H^{s+1/2}(\Omega)$ for $s \in (0, 1]$. For instance, one can take

$$\mathrm{R}_{\Sigma\Omega} g_\Sigma := u, \quad \text{with } u \text{ satisfying } \Delta u = 0, \quad \gamma_\Sigma u = g_\Sigma,$$

the Dirichlet solution for the Laplace operator. Such operator is continuous, not only for $s \in (0, 1)$, but it attains the end point $s = 1$ as well (cf. [30, Chapter 6]; see Theorem 6.12 and the discussion following it).

We are ready to define the desired projection on the finite element space on the boundary $\gamma_\Sigma \mathbb{P}_{h,d}$. To this end, we first set

$$\mathrm{P}^h_\Sigma := \gamma_\Sigma \Pi_h \mathrm{R}_{\Sigma\Omega}.$$

Proposition A.3. *Let $\mathrm{P}^h_\Sigma : H^s(\Sigma) \to \gamma_\Sigma \mathbb{P}_{h,d}$ as above. Then*

$$\|\mathrm{P}^h_\Sigma f_\Sigma - f_\Sigma\|_{H^s(\Sigma)} \leq C h_\Sigma^{t-s} \|f_\Sigma\|_{H^t(\Sigma)}, \quad 0 \leq s < 1, \quad s \leq t < d+1, \quad t > 0, \tag{A.7}$$

where C is independent of f_Σ and h. Furthermore, for any $s \in [0, 1)$ and $t > d+1$, there exists $C > 0$ such that

$$\|\mathrm{P}^h_\Sigma f_\Sigma - f_\Sigma\|_{H^s(\Sigma)} \leq C h_\Sigma^{d+1-s} \|f\|_{H^t(\Sigma)}. \tag{A.8}$$

Proof. By construction, Π_h is a projection. Indeed, if $\mathrm{Q}_h : \mathcal{C}(\Omega) \to \mathbb{P}_{h,d}$ is the nodal $d-$Lagrange interpolation operator, and since $\gamma_\Sigma \mathrm{Q}_h = \mathrm{Q}^h_\Sigma \gamma_\Sigma$, we have that

$$\gamma_\Sigma \Pi_h \mathrm{R}_{\Sigma\Omega} f^h_\Sigma - f^h_\Sigma \;=\; \gamma_\Sigma (\Pi_h - \mathrm{Q}_h) \mathrm{R}_{\Sigma\Omega} f^h_\Sigma = \gamma_\Sigma \Pi_h \underbrace{(\mathrm{I} - \mathrm{Q}_h) \mathrm{R}_{\Sigma\Omega} f^h_\Sigma}_{\in H^1_0(\Omega)} = 0$$

by (A.4b).

On the other hand, for $t \in (1/2, 1]$ with $t \geq s$, and $s \in (0, 1)$, and by the continuity of the trace operator,

$$\begin{aligned} \|\mathrm{P}^h_\Sigma f_\Sigma - f_\Sigma\|_{H^s(\Sigma)} &\leq C\|\Pi_h \mathrm{R}_{\Sigma\Omega} f_\Sigma - \mathrm{R}_{\Sigma\Omega} f_\Sigma\|_{H^{s+1/2}(\Omega)} \\ &\leq C' h_\Sigma^{t-s} \|\mathrm{R}_{\Omega\Sigma} f_\Sigma\|_{H^{t+1/2}(\Omega)} \leq C'' h_\Sigma^{t-s} \|f_\Sigma\|_{H^t(\Sigma)}. \end{aligned} \tag{A.9}$$

To prove the estimate in $H^0(\Sigma) = L^2(\Sigma)$ we recall the trace inequality cf [4, Th. 1.6.6]

$$\|\gamma_\Sigma u\|^2_{L^2(\Sigma)} \leq C\big(\|u\|^2_{L^2(\Omega)} + \|u\|_{L^2(\Omega)}\|u\|_{H^1(\Omega)}\big) \leq C(1 + \tfrac{1}{2}h_\Sigma^{-1})\|u\|^2_{L^2(\Omega)} + \tfrac{1}{2}Ch_\Sigma\|u\|^2_{H^1(\Omega)}$$

which yields

$$\begin{aligned} \|\mathrm{P}^h_\Sigma f_\Sigma - f_\Sigma\|_{L^2(\Sigma)} &\leq Ch_\Sigma^{1/2}\|\Pi_h \mathrm{R}_{\Omega\Sigma} f_\Sigma - \mathrm{R}_{\Omega\Sigma} f_\Sigma\|_{H^1(\Omega)} + Ch_\Sigma^{-1/2}\|\Pi_h \mathrm{R}_{\Omega\Sigma} f_\Sigma - \mathrm{R}_{\Omega\Sigma} f_\Sigma\|_{H^0(\Omega)} \\ &\leq C' h_\Sigma^t \|\mathrm{R}_{\Omega\Sigma} f_\Sigma\|_{H^{t+1/2}(\Omega)} \leq C' h_\Sigma^t \|f_\Sigma\|_{H^t(\Sigma)}. \end{aligned}$$

We have then proved (A.7) for $0 \leq s < 1$ and $\max\{s, 1/2\} < t \leq 1$ and therefore it only remains to extend this result for $t > 1$. But,

$$\|\mathrm{P}^h_\Sigma f_\Sigma - f_\Sigma\|_{H^s(\Sigma)} = \|\mathrm{P}^h_\Sigma(f_\Sigma - \mathrm{Q}^h_\Sigma f) - (f_\Sigma - \mathrm{Q}^h_\Sigma f)\|_{H^s(\Sigma)} \leq Ch_\Sigma^{1-s}\|f_\Sigma - \mathrm{Q}^h_\Sigma f_\Sigma\|_{H^1(\Sigma)}$$

and the result follows from Proposition A.1.

□

Note that, using the above arguments, (A.7) cannot be extended to $s = 1$.

A.2 Commutator properties for Scott-Zhang projections

We end this section showing a commutation property for Π_h. We stress out that the result is also valid in 3D for tetrahedral meshes with minor but direct modifications.

Lemma A.4. *For any $\varpi \in \mathcal{C}^\infty(\Omega)$ there exists $C > 0$ so that for $d \geq 2$ and $s \in [0, 3/2)$*

$$\|\Pi_h(\varpi w_h) - \varpi w_h\|_{H^s(\Omega)} \leq Ch\|w_h\|_{H^s(\Omega)}, \quad \forall w_h \in \mathbb{P}_{h,d}.$$

For $d = 1$ (linear finite elements), we have instead

$$\|\Pi_h(\varpi w_h) - \varpi w_h\|_{H^s(\Omega)} \leq Ch^{\min\{1,2-s\}}\|w_h\|_{H^s(\Omega)}, \quad \forall w_h \in \mathbb{P}_{h,1}.$$

Proof. Consider $\mathrm{Q}_h : \mathcal{C}^0 \to \mathbb{P}_{h,d}$ the classical nodal interpolant on $\mathbb{P}_{h,d}$ which satisfies

$$\|u - \mathrm{Q}_h u\|_{H^s(T)} \leq C_{s,t} h_T^{t-s}\|u\|_{H^t(T)}, \qquad \forall T \in \mathcal{T}_h \tag{A.10}$$

for any $0 \leq s < 3/2$, and $s \leq t \leq d + 1$ with $t > 1$ for triangular meshes in bidimensional polygonal domains ($t > 3/2$ for 3D polygonal domains). In (A.10), h_T is the diameter of the element T, and $C_{s,t}$ is a constant independent of T and u_h.

Recall also the inverse inequalities which hold locally on each triangle:

$$\|w_h\|_{H^s(T)} \leq C_{s,t} h_T^{t-s}\|w_h\|_{H^t(T)}, \quad \forall w_h \in \mathbb{P}_{h,d} \tag{A.11}$$

with C depending again only on d, $s \geq t$ and the chunkiness parameter of the grid. Then, locally on each element it holds

$$\|\varpi w_h\|_{H^{d+1}(T)} \leq C_\varpi \|w_h\|_{H^{d+1}(T)} = C_\varpi \|w_h\|_{H^d(T)} \leq C'_{\varpi,s} h_T^{s-d-1} \|w_h\|_{H^s(T)}$$

for any $s \in [0, d]$.

We start with the $s \in [0, 1/2)$ case. Using (A.5), the convergence properties of Π_h (A.4d), the interpolant operator Q_h and the inverse inequality (A.11),

$$\begin{aligned}
\|\Pi_h(\varpi w_h) - \varpi w_h\|^2_{H^s(\Omega)} & \\
&\leq C_s \sum_{T\in\mathcal{T}_h} \|\Pi_h(\varpi w_h - \mathrm{Q}_h(\varpi w_h)) - (\varpi w_h - \mathrm{Q}_h(\varpi w_h))\|^2_{H^s(T)} \\
&\leq C'_s \sum_{T\in\mathcal{T}_h} h_T^{2-2s} \|\varpi w_h - \mathrm{Q}_h(\varpi w_h)\|^2_{H^1(T)} \leq C'_s \sum_{T\in\mathcal{T}_h} h_T^{2d+2-2s} \|\varpi w_h\|^2_{H^{d+1}(T)} \\
&\leq C''_{s,\varpi} \sum_{T\in\mathcal{T}_h} h_T^2 \|w_h\|^2_{H^s(T)} \leq C'_{s,\varpi} h^2 \|w_h\|^2_{H^s(\Omega)}.
\end{aligned}$$

For $s \in [1, 3/2)$, we proceed in a similar manner: Using the stability of the Scott-Zhang type projection

$$\begin{aligned}
\|\Pi_h(\varpi w_h) - \varpi w_h\|^2_{H^s(\Omega)} &\leq C_s \|\mathrm{Q}_h(\varpi w_h) - \varpi w_h\|^2_{H^s(\Omega)} \\
&\leq C'_s \sum_{T\in\mathcal{T}_h} h_T^{2d-2s} \|\varpi w_h\|^2_{H^{d+1}(T)} \leq C_{s,\varpi} \sum_{T\in\mathcal{T}_h} h_T^{2d-2s} \|w_h\|^2_{H^d(T)}.
\end{aligned}$$

The result follows now using either the direct bound

$$\|w_h\|_{H^d(T)} \leq \|w_h\|_{H^s(T)}, \quad \text{for } d = 1,$$

or the inverse inequality (A.11) for $d \geq 2$.

We have then proven the result for $s \in [0, 1/2) \cup [1, 3/2)$. For the intermediate values of $s \in (1/2, 1)$ we just invoke the Interpolation Theory of Sobolev spaces. □

Remark A.5. We note that in [2] the weaker estimate is proven:

$$\|\Pi_h(\varpi v_h) - \varpi v_h\|_{H^s(\Omega)} \leq C h^s \|v_h\|_{H^s(\Omega)}, \quad \forall v_h \in \mathbb{P}_{h,d}$$

for $s \in (1/2, 1]$ and for any projection on finite element spaces satisfying rather general assumptions which include, in particular, our case.

B Convergence/superconvergence of FEM in stronger norms

In this appendix Ω is a polygonal domain with boundary Σ in both $\mathbb{R}^m$ with $m = 2, 3$ and

$$b_{n,\Omega}(u, v) := (\nabla u, \nabla v)_\Omega - (u, v)_{n,\Omega} := \int_\Omega \nabla u \cdot \nabla v - \int_\Omega n\, uv$$

is the bilinear form associated to the Dirichlet problem

$$\left| \begin{array}{rcl} \Delta u + nu & = & f \\ \gamma_\Sigma u & = & g_\Sigma. \end{array} \right.$$

Here $1-n$ is a L^2-function with compact support Ω_0 in Ω. As before we consider a sequence of regular grids made up of conformal triangular/tetrahedral elements $\mathcal{T}_h$. The parameter h refers again to the maximum of the diameters of the elements in such a way that we write $h \to 0$ to mean that the diameters of the elements tend to zero. On $\mathcal{T}_h$ we construct a continuous finite element space of the elements which are polynomials of degree d on each $T \in \mathcal{T}_h$ and denote it by $\mathbb{P}_{h,d}$.

We will work with the numerical solution given by the usual FEM scheme:

$$\left|\begin{array}{rcl} u_h \in \mathbb{P}_{h,d} & & \\ b_{n,\Omega}(u_h, v_h) & = & -(f, v_h)_\Omega, \quad \forall v_h \in \mathbb{P}_{h,d} \cap H_0^1(\Omega) \\ \gamma_\Sigma u & = & g_\Sigma^h. \end{array}\right.$$

Here, $\gamma_\Sigma \mathbb{P}_{h,d} \ni g_\Sigma^h \approx g_\Sigma$. Some preliminary results can be listed at this point. Provided that $g_\Sigma \in H^{1/2}(\Sigma)$, $f \in L^2(\Omega)$ then $u \in H^1(\Omega)$ with

$$\|u\|_{H^1(\Omega)} \leq C\big(\|f\|_{L^2(\Omega)} + \|g_\Sigma\|_{H^{1/2}(\Sigma)}\big).$$

We recall the standard error result [11, 37]

$$\|u - u_h\|_{H^1(\Omega)} \leq C\Big[\inf_{v_h \in \mathbb{P}_{h,d}} \|u - v_h\|_{H^1(\Omega)} + \|g_\Sigma - g_\Sigma^h\|_{H^{1/2}(\Omega)}\Big]$$

which gives us a convergence estimate in the natural norm. We however want to explore convergence estimates in stronger norms in the subdomains where the solution u is more regular. The following theorem presents the main result of this appendix. The proof of this result uses similar ideas as those presented in [32] for proving superconvergence in H^1 for a more general class of partial differential equations. We include it in this work for the sake of completeness.

Theorem B.1. *Let D', D be two domains with $D' \subset \overline{D}' \subset D \subset \overline{D} \subset \Omega \setminus \Omega_0$ and let $\{\mathcal{T}_h\}$ be a sequence of regular grids with $h \to 0$ which are quasi-uniform in D' cf. (4.9). Then for any $\varepsilon \in [0, 1/2)$, $u \in H^{r+1}(D')$ with $r \in [\varepsilon, d]$, there exists $C > 0$ depending on ε, r, D, D' so that for any grid fine enough $\mathcal{T}_h$ it holds*

$$\|u - u_h\|_{H^{1+\varepsilon}(D')} \leq C\big[h_D^{-\varepsilon}\|u - u_h\|_{H^0(D)} + h_D^{r-\varepsilon}\|u\|_{H^{r+1}(D)} + h_D^{1-\varepsilon}\|u - u_h\|_{H^1(D)}\big] \tag{B.1}$$

where h_D is the maximum of the diameters of the elements contained in D.

Proof. Let Π_h be a Scott-Zhang type projection satisfying (A.4), and hence the commutator property stated in Lemma A.4. Take a smooth cut-off function ϖ satisfying

$$\begin{array}{c} \varpi|_{D'} \equiv 1, \quad \operatorname{supp} \varpi \subset D, \\ \Pi_h(\varpi v_h)|_{D'} = v_h|_{D'}, \quad \forall v_h \in \mathbb{P}_{h,d}, \quad \Pi_h(\varpi v)|_D \in H_0^1(D), \quad \forall v \in H^1(D). \end{array} \tag{B.2}$$

We consider the $H^1(D)$ inner product

$$\beta_D(u, v) := (\nabla u, \nabla v)_D + (u, v)_D,$$

and set

$$e_h := u - u_h, \quad \widetilde{e}_h := \Pi_h(\varpi u) - \Pi_h(\varpi u_h) \in \mathbb{P}_{h,d}, \quad \widetilde{e}^h := \varpi u - \Pi_h(\varpi u).$$

Using (B.2),

$$\varpi e_h|_{D'} = (\widetilde{e}_h + \widetilde{e}^h)|_{D'}. \tag{B.3}$$

Then

$$\|e_h\|_{H^{1+\varepsilon}(D')} \leq \|\varpi e_h\|_{H^{1+\varepsilon}(D)} \leq \|\widetilde{e}_h\|_{H^{1+\varepsilon}(D)} + \|\widetilde{e}^h\|_{H^{1+\varepsilon}(D)}, \tag{B.4}$$

For bounding the first term we start applying the inverse inequality

$$\|\widetilde{e}_h\|_{H^{1+\varepsilon}(D)} \leq C_\varepsilon h_D^{-\varepsilon}\|\widetilde{e}_h\|_{H^1(D)} = C_\varepsilon h_D^{-\varepsilon}\beta_D(\widetilde{e}_h, v_h), \quad \text{with } v_h = \frac{1}{\|\widetilde{e}_h\|_{H^1(D)}}\widetilde{e}_h \in \mathbb{P}_{h,d} \cap H_0^1(D), \tag{B.5}$$

and continue applying the decomposition

$$\widetilde{e}_h = (\varpi u - \varpi u_h) + (\Pi_h - \mathrm{I})(\varpi u - \varpi\Pi_h u) + (\Pi_h - \mathrm{I})(\varpi\Pi_h u - \varpi u_h).$$

Hence,

$$\begin{aligned}
\|\widetilde{e}_h\|_{H^{1+\varepsilon}(D)} &\leq C_\varepsilon h_D^{-\varepsilon}\Big(\beta_D(\varpi u - \varpi u_h, v_h) + \beta_D((\Pi_h - \mathrm{I})(\varpi u - \varpi\Pi_h u), v_h) \\
&\quad + \beta_D((\Pi_h - \mathrm{I})(\varpi\Pi_h u - \varpi u_h), v_h)\Big) \\
&\leq C_\varepsilon h_D^{-\varepsilon}\Big(\beta_D(\varpi e_h, v_h) + \|(\Pi_h - \mathrm{I})(\varpi u - \varpi\Pi_h u)\|_{H^1(D)} \\
&\quad + \|(\Pi_h - \mathrm{I})(\varpi\Pi_h u - \varpi u_h)\|_{H^1(D)}\Big) \\
&\leq C_\varepsilon h_D^{-\varepsilon}\big(\beta_D(\varpi e_h, v_h) + \|\varpi u - \varpi\Pi_h u\|_{H^1(D)} + h_D\|(\Pi_h u - u) + (u - u_h)\|_{H^1(D)}\big) \\
&\leq C_\varepsilon h_D^{-\varepsilon}\big(\beta_D(\varpi e_h, v_h) + \|\Pi_h u - u\|_{H^1(D)} + h_D\|e_h\|_{H^1(D)}\big),
\end{aligned} \tag{B.6}$$

where to bound the last term, we used the the commutator property, cf. Lemma A.4 with $w_h = \Pi_h u - u_h$. Next, we consider the first term in (B.6) and obtain a bounding estimate. Observe that

$$\begin{aligned}
\beta_D(\varpi e_h, v_h) &= \int_D e_h\nabla\varpi\cdot\nabla v_h - \int_D v_h\nabla e_h\cdot\nabla\varpi + \beta_D(e_h, \varpi v_h) \\
&= 2\int_D e_h\nabla\varpi\cdot\nabla v_h + \int_D v_h e_h\Delta\varpi \\
&\quad + \beta_D(e_h, \varpi v_h - \Pi_h(\varpi v_h)) + \beta_D(e_h, \Pi_h(\varpi v_h)).
\end{aligned}$$

Thus, and after applying again Lemma A.4 to the third term above,

$$\beta_D(\varpi e_h, v_h) \leq C\|e_h\|_{L^2(D)} + Ch_D\|e_h\|_{H^1(D)} + \beta_D(e_h, \Pi_h(\varpi v_h)). \tag{B.7}$$

Finally, using the orthogonality relation for the Galerkin solution,

$$\begin{aligned}
\beta_D(e_h, \Pi_h(\varpi v_h)) &= \underbrace{\int_\Omega \nabla e_h\cdot\nabla\Pi_h(\varpi v_h) - \int_\Omega n\, e_h\Pi_h(\varpi v_h)}_{=0} + \int_D (1+n)e_h\Pi_h(\varpi v_h) \\
&\leq C\|e_h\|_{L^2(D)}\|\varpi v_h\|_{L^2(\Omega)} \leq C\|e_h\|_{L^2(D)}.
\end{aligned} \tag{B.8}$$

Plugging (B.8) in (B.7) and next (B.7) in (B.6) yield

$$\|\widetilde{e}_h\|_{H^{1+\varepsilon}(D')} \leq Ch_D^{-\varepsilon}\big(\|e_h\|_{L^2(D)} + \|\Pi_h u - u\|_{H^1(D)} + h_D\|e_h\|_{L^2(D)}\big) \tag{B.9}$$

Therefore, (B.9) with (B.4) prove

$$\begin{aligned}\|e_h\|_{H^{1+\varepsilon}(D')} \leq C_\varepsilon\big(&h_D^{-\varepsilon}\|e_h\|_{L^2(D)} + h_D^{1-\varepsilon}\|e_h\|_{H^1(D)} \\ &+ h_D^{-\varepsilon}\|\Pi_h u - u\|_{H^1(D)} + \|\Pi_h(\omega u) - \omega u\|_{H^{1+\varepsilon}(D)}\big),\end{aligned} \tag{B.10}$$

for any $\varepsilon \in [0, 1/2)$. The result follows readily from the convergence estimates for Π_h.

□

A convergence estimate in $L^2(\Omega)$ is needed to obtain a convergence result of the finite element solution in D. This is done next using a variant of the classical Aubin-Nische argument

Lemma B.2 (Aubin-Nitsche trick)**.** *Then for $\delta \in (1/2, 1]$ it holds*

$$\|u - u_h\|_{L^2(\Omega)} \leq C\Big[h^\delta \|u - u_h\|_{H^1(\Omega)} + \|g_\Sigma - g_\Sigma^h\|_{L^2(\Sigma)}\Big]$$

where h denotes the maximum of the diameters of the elements of the mesh $\mathcal{T}_h$ of Ω.

Proof. Let us denote as before $e_h := u - u_h$ and take w the (unique) solution of

$$\left|\begin{array}{l} w \in H_0^1(\Omega) \\ \Delta w + n\, w = -e_h \end{array}\right. \quad \text{or in variational form,} \quad \left|\begin{array}{l} w \in H_0^1(\Omega) \\ b_{\Omega,n}(w, v) = (e_h, v)_\Omega, \quad \forall v \in H_0^1(\Omega). \end{array}\right.$$

It is known that there exists $\delta \in (1/2, 1]$ such that

$$\|w\|_{H^{1+\delta}(\Omega)} \leq C_\delta \|e_h\|_{L^2(\Omega)}$$

with C_δ independent of e_h.

Then

$$\begin{aligned}\|e_h\|_{L^2(\Omega)}^2 &= (e_h, e_h)_\Omega = -(\Delta w + n\, w, e_h)_\Omega \\ &= b_{\Omega,n}(w, e_h) + \int_\Sigma \partial_n w\, e_h = b_{\Omega,n}(w - \Pi_h w, e_h) + \int_\Sigma \partial_n w\, e_h\end{aligned}$$

where we have made use of the Galerkin orthogonality of the discrete solution and the fact that $\Pi_h w \in \mathbb{P}_{h,d} \cap H_0^1(\Omega)$ for $w \in H_0^1(\Omega)$. Notice that from the trace theorem

$$\|\partial_n w\|_{L^2(\Sigma)} \leq \|\gamma_\Sigma \nabla w\|_{L^2(\Sigma)} \leq C\|w\|_{H^{1+\delta}(\Omega)}.$$

Therefore,

$$\begin{aligned}\|e_h\|_{L^2(\Omega)}^2 &\leq C\big[\|w - \Pi_h w\|_{H^1(\Omega)}\|e_h\|_{H^1(\Omega)} + \|w\|_{H^{1+\delta}(\Omega)}\|e_h\|_{L^2(\Sigma)}\big] \\ &\leq C'\big[h^\delta\|e_h\|_{H^1(\Omega)} + \|g_\Sigma - g_\Sigma^h\|_{L^2(\Sigma)}\big]\|w\|_{H^{1+\delta}(\Omega)} \\ &\leq C''\big[h^\delta\|e_h\|_{H^1(\Omega)} + \|g_\Sigma - g_\Sigma^h\|_{L^2(\Sigma)}\big]\|e_h\|_{L^2(\Omega)}.\end{aligned}$$

The proof is now completed. □

The parameter δ in Lemma B.2 is nothing but the extra regularity grade, from a Sobolev point of view, of the homogeneous Dirichlet problem

$$\Delta w + n\, w = g, \quad \gamma_\Sigma w = 0.$$

It is a very well established result, see for instance [20], that $\delta \in (1/2, 1]$ and it attains to be 1 for convex polygons in $\mathbb{R}^2$.

Corollary B.3. *Under the same assumptions as those taken in Theorem B.1 and Lemma B.2, we have that for any* $\varepsilon \in [0, 1/2)$

$$\|u - u_h\|_{H^{1+\varepsilon}(D')} \leq C\big((h^{\delta} h_D^{-\varepsilon} + h_D^{1-\varepsilon})\|u - u_h\|_{H^1(\Omega)} + h_D^{-\varepsilon}\|g_\Sigma - g_\Sigma^h\|_{L^2(\Sigma)} + h_D^{r-\varepsilon}\|u\|_{H^{r+1}(D)}\big).$$

In particular, if $h^{\delta} h_D^{-\varepsilon} \to 0$ *and* g_Σ^h *is taken satisfying*

$$h_D^{-\varepsilon}\|g_\Sigma - g_\Sigma^h\|_{L^2(\Sigma)} \leq C(h)\|g_\Sigma - g_\Sigma^h\|_{H^{1/2}(\Sigma)}$$

with $C(h) \to 0$ *as* $h \to 0$*, there exists* $\eta(h)$ *with* $\eta(h) \to 0$ *as* $h \to 0$ *such that*

$$\|u - u_h\|_{H^{1+\varepsilon}(D')} \leq \eta(h)\big(\inf_{v_h \in \mathbb{P}_{h,d}} \|u - v_h\|_{H^1(\Omega)} + \|g_\Sigma - g_\Sigma^h\|_{H^{1/2}(\Sigma)}\big). \tag{B.11}$$